remote sensing

MDPI

Article

Aerosol Optical and Microphysical Characteristics Related to Vertical Distribution over Korea Using Aerosol Scale Height

Chang Ki Kim [1,2], Hyun-Goo Kim [1,2,*], Myeongchan Oh [1], Min-Gu Kang [1] and Youngseok Bak [1]

[1] Renewable Energy Big Data Laboratory, Korea Institute of Energy Research, Daejeon 34129, Republic of Korea; ckkim@kier.re.kr (C.K.K.); amir117@kier.re.kr (M.O.); mgkang@kier.re.kr (M.-G.K.); bhybyk@kier.re.kr (Y.B.)
[2] Energy Engineering, University of Science and Technology, Daejeon 34113, Republic of Korea
* Correspondence: hyungoo@kier.re.kr; Tel.: +82-42-860-3376

Highlights

What are the main findings?

- Aerosol scale height frequently differs from planetary boundary layer height, with the highest relative values in spring and the lowest in autumn.
- A larger aerosol scale height relative to the boundary layer is associated with a lower Ångström exponent, enhanced coarse-mode volume, and higher single scattering albedo, while surface PM_{10} shows only a weak relationship.

What are the implications of the main findings?

- The comparison between aerosol scale height and planetary boundary layer height provides a practical indicator of changes in aerosol vertical distribution and surface–column coupling.
- Column-integrated optical and microphysical properties can reveal vertically decoupled aerosol conditions that are not fully represented by surface particulate measurements.

Abstract

Aerosol optical depth characterizes total aerosol loading in the atmospheric column but does not directly indicate its vertical distribution relative to the planetary boundary layer. This study investigates aerosol vertical structure over Daejeon, Korea, by integrating column aerosol optical properties from a sky radiometer, near-surface atmospheric extinction measurements, and planetary boundary layer height from reanalysis data. Aerosol scale height is derived from aerosol optical depth at 870 nm and near-surface extinction and is analyzed alongside aerosol optical and microphysical properties. Aerosol scale height exhibits substantial variability relative to the planetary boundary layer height, with the highest relative values occurring in spring and the lowest in autumn. An increase in aerosol scale height relative to the boundary layer is accompanied by a decrease in the Ångström exponent and an increase in the coarse-mode volume fraction. The coarse-mode enhancement is driven mainly by an increase in coarse-mode aerosol volume, whereas surface PM_{10} concentrations show only a weak relationship with variations in vertical structure. Single scattering albedo generally increases, indicating a more scattering dominated column aerosol population. These results demonstrate that combining aerosol scale height with planetary boundary layer height provides valuable information on aerosol vertical structure and the degree of correspondence between surface and column aerosol conditions.

Keywords: aerosol scale height; planetary boundary layer height; aerosol vertical structure; aerosol optical properties; aerosol size distribution

Check for updates

Academic Editors: Disong Fu, Kai Wu, Hongrong Shi and Yu Zheng

Received: 9 September 2026
Revised: 20 October 2026
Accepted: 21 October 2026
Published: 22 October 2026

Copyright: © 2026 by the authors. Licensee MDPI, Basel, Switzerland. This article is an open access article distributed under the terms and conditions of the Creative Commons Attribution (CC BY) license.

1. Introduction

Atmospheric aerosols modulate the energy balance of the Earth–atmosphere system by scattering and absorbing solar radiation and by altering cloud microphysical and radiative properties, and they simultaneously act as the dominant controls on visibility degradation, surface air quality, and the availability of the solar resource at the ground [1–5]. Because the magnitude of these effects depends jointly on aerosol loading, particle size, and absorbing capacity, aerosol radiative forcing remains the largest single source of uncertainty in assessing anthropogenic climate change. For example, the Sixth Assessment Report of the Intergovernmental Panel on Climate Change assessed the total aerosol effective radiative forcing over the industrial era as -1.3 W m^{-2} with a very likely range of -2.0 to -0.6 W m^{-2}, an uncertainty range that is considerably wider than that of well-mixed greenhouse gases [1]. Aerosols also provide feedback on the state of the lower atmosphere itself: Li et al. [2] showed that absorbing aerosols warm the upper part of the boundary layer while reducing the surface radiative flux, thereby stabilizing the layer, suppressing turbulent mixing, and further concentrating pollutants near the surface. This two-way coupling between aerosol loading and boundary-layer structure implies that aerosol optical properties and the vertical structure of the lower atmosphere cannot be interpreted independently.

These processes are particularly pronounced over East Asia, where dense anthropogenic emissions coexist with one of the most active mineral dust source regions in the world, and where the Korean Peninsula is located immediately downwind of the prevailing westerly transport pathway [4–11]. Ground-based and satellite observations over the region consistently indicate a springtime maximum in column aerosol loading associated with transported dust and a marked reduction from mid-autumn to mid-winter, together with pronounced seasonal changes in column particle size and absorption characteristics. For example, long-term sky-radiometer measurements at East Asian SKYNET sites showed higher aerosol optical depth (AOD) and lower Ångström exponent (AE) in spring than in autumn, reflecting an increased coarse-mode contribution during the dust season [4], while Chun et al. [7] documented, based on both historical and modern Korean records, that Asian dust events occur overwhelmingly between March and May and are essentially absent in summer. At the same time, sustained emission controls have produced a long-term decline in surface particulate matter over Korea, with annual mean PM_{10} decreasing by approximately 36% between 1998 and 2023 and $PM_{2.5}$ decreasing from 26 to 19 μg m^{-3} between 2015 and 2023 [12]. The coexistence of a declining local anthropogenic background with an episodic, externally supplied coarse-mode contribution makes the relationship between surface and column aerosol conditions over Korea particularly variable, and therefore worthy of explicit quantification.

A fundamental limitation in this context is that AOD is a vertically integrated quantity and therefore provides no direct information about how aerosol extinction is distributed with altitude. Two atmospheric columns with identical AOD may correspond to aerosol confined within a shallow, stably stratified surface layer, dispersed through a deep mixed layer, or present as an elevated plume that is dynamically decoupled from the surface altogether. Because surface particulate matter concentrations respond to the near-surface portion of the profile whereas AOD responds to the entire column, the correspondence between the two is strongly influenced by the depth over which aerosols are distributed relative to the planetary boundary layer height (PBLH) [13–17]. One compact way of expressing this vertical extent is the aerosol scale height (ASH), defined as the ratio of column AOD to the near-surface aerosol extinction coefficient, representing the equivalent depth of a vertically uniform layer that would reproduce the observed column loading. Because ASH requires only a column AOD measurement and a co-located near-surface extinction measurement, it provides an inexpensive proxy for the effective vertical extent

of aerosol optical loading, and comparing ASH with an independently diagnosed PBLH offers a direct measure of the degree of surface–column aerosol coupling.

ASH and, more generally, aerosol vertical structure have been investigated using a variety of approaches, including sun-photometer and visibility combinations, elastic-backscatter and Raman lidar, spaceborne lidar, and airborne in situ profiling [10,11,13–22]. For example, Qiu et al. [18] established that a scaling height and an exponential-type extinction profile can be retrieved from pyrheliometer or sun-photometer measurements combined with surface visibility data, and demonstrated substantial seasonal variability in the retrieved scaling height over China. Shin and Lee [19] applied the same principle at Gwangju, Korea, obtaining springtime scaling heights ranging from 0.39 to 3.55 km, and found that the resulting extinction profiles agreed well with co-located lidar observations except under dust-dominated conditions, when uplifted layers above the boundary layer could not be represented by a single vertically uniform scale. Chew et al. [14] further showed that normalizing AOD by a lidar-derived ASH improved the explained variance in AOD–$PM_{2.5}$ relationships by 5–11%, confirming that the effective aerosol vertical extent is a first-order control of surface–column consistency. Nevertheless, several important limitations persist. Studies that resolve the vertical profile directly rely on lidar, spaceborne lidar, or aircraft observations, which are expensive, spatially sparse, restricted to short intensive campaigns, or limited by satellite sampling frequency, and are therefore unavailable at the vast majority of routine monitoring sites [11,20]. Studies that derive ASH from ground-based measurements alone have generally been confined to short periods, selected dust episodes, or evaluation of the retrieved profile shape itself, and have rarely examined ASH over multiple years. Most importantly, previous work has treated ASH primarily as an intermediate quantity for reconstructing extinction profiles or correcting AOD–PM relationships, and the question of how departures of ASH from PBLH relate to the column aerosol optical and microphysical properties themselves—including size distribution, coarse-mode contribution, and single scattering albedo—has received little attention. In addition, the PBLH used in such comparisons is typically obtained from reanalysis, which is known to exhibit systematic differences from lidar-derived boundary-layer heights over East Asia [22]; therefore, the interpretation of any ASH–PBLH relationship must be framed as a relative rather than an absolute diagnostic.

The present study addresses these gaps using a multi-year, entirely ground-based observational configuration at Daejeon, Korea. In contrast to previous studies that relied on lidar or airborne profiling to characterize aerosol vertical structure, ASH is derived here from column AOD at 870 nm measured by a sky radiometer and the near-surface extinction coefficient measured by a visibility sensor at approximately 850 nm, thereby eliminating the need for active remote sensing. The dimensionless ratio of ASH to PBLH is then used as a quantitative indicator of surface–column aerosol coupling, and its monthly and seasonal behavior is characterized over the period from May 2023 to January 2026. The novel aspect of the analysis is that the ASH–PBLH ratio is examined jointly with the column-integrated optical and microphysical properties retrieved from the same instrument—including AE between 400 and 870 nm, the volume size distribution and the resulting fine- and coarse-mode volumes, and spectral single scattering albedo—as well as with co-located surface PM_{10} concentrations. This combination makes it possible to test whether an increasing divergence between the effective AOD scale and the meteorological mixing depth is accompanied by a systematic change in the characteristics of the column aerosol population, and whether such conditions are detectable using surface particulate measurements. The specific objectives are therefore to (i) quantify the monthly and seasonal variability of ASH relative to PBLH over Korea, (ii) establish how columnar aerosol size and absorption properties vary with the ratio of ASH to PBLH, (iii) assess the extent to which surface PM_{10}

reflects these column-scale changes, and (iv) evaluate whether this ratio can also serve as a practical, low-cost indicator of aerosol vertical structure and surface–column decoupling obtainable from routine ground-based observations. Section 2 describes the observational datasets, data processing procedures, and methods used to derive ASH and characterize the aerosol vertical structure. Section 3 presents the temporal and seasonal characteristics of aerosol optical properties, ASH, PBLH, and their relative variability. Section 4 discusses the relationships between aerosol vertical structure and aerosol optical and microphysical properties, including particle-size characteristics and surface–column coupling. Finally, Section 5 summarizes the principal findings and key conclusions of this study.

2. Data and Methodology

2.1. Study Site and Observation Period

The geographical setting of the study region and the observation sites is shown in Figure 1. All measurements analyzed in this study are conducted at, or in the immediate vicinity of, the Korea Institute of Energy Research (KIER) in Daejeon, Republic of Korea (36.3840° N, 127.3596° E; elevation ≈ 55 m above mean sea level; red circle in Figure 1). Daejeon is the fifth-largest metropolis in the Republic of Korea, with a population of approximately 1.44 million and an area of approximately 540 km^2, and it is located in the inland central part of the Korean Peninsula, roughly 140 km south of the Seoul metropolitan area and approximately 60 km east of the Yellow Sea coast. The city occupies a complex basin bounded by low mountain ranges, a topographic configuration that restricts horizontal ventilation and favors the accumulation of locally emitted pollutants during periods of weak synoptic forcing; over the Korean Peninsula, such basin terrain has been shown to coincide with reduced atmospheric ventilation and elevated particulate matter concentrations [23].

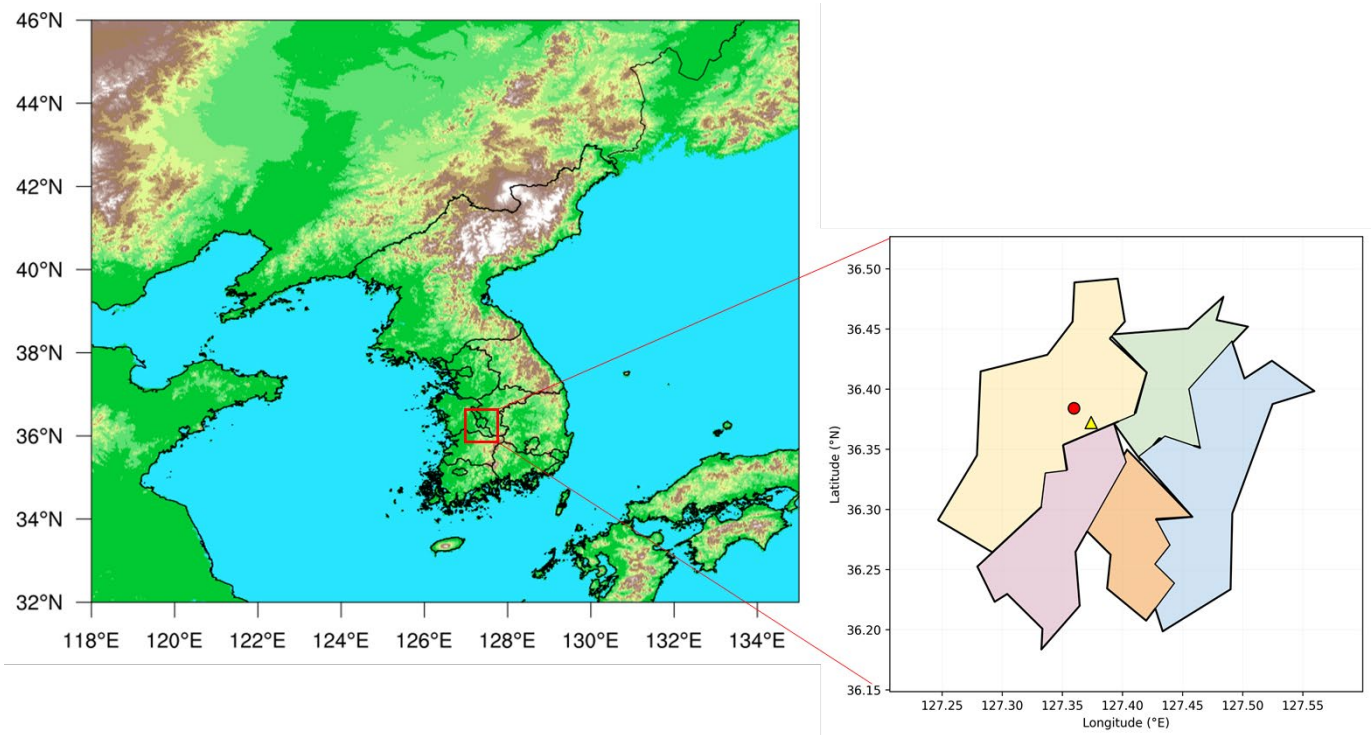


Figure 1. Study area. Red circle and yellow triangle indicate the location of the Korea Institute of Energy Research and the Daejeon Metropolitan City Institute of Health and Environment, respectively. Colors in subplot indicate the different district in Daejeon Metropolitan City.

Surface particulate matter concentrations are obtained from the air quality monitoring station operated by the Daejeon Metropolitan City Institute of Health and Environment

(36.3723° N, 127.3740° E; yellow triangle in Figure 1), located approximately 1.8 km southeast of the KIER site. Given this short separation distance and the absence of intervening topographic barriers or major isolated sources, the two locations are assumed to sample a similar near-surface air mass on the hourly time scale considered here, and the monitoring station is therefore treated as effectively co-located with the optical measurements.

The observation period evaluated in this study spans from 1 May 2023 to 30 January 2026, covering approximately 33 months and thereby encompassing three complete spring dust seasons and three summer monsoon periods. All variables are synchronized to a common hourly resolution in Local Standard Time (LST = UTC + 9 h) to ensure consistency among the surface, column-integrated, and reanalysis quantities. Because the retrieval of column-integrated aerosol properties requires direct solar irradiance, the analysis is intrinsically restricted to cloud-free daytime hours, and this sampling constraint is considered when interpreting the derived statistics. The individual instruments, retrieval algorithms, quality-control procedures, and reanalysis product used to obtain these quantities are described in Section 2.2.

2.2. Observational and Reanalysis Datasets

2.2.1. Surface Extinction and PM Concentrations

Near-surface atmospheric extinction is measured using a CS125 visibility and present weather sensor (Campbell Scientific, Logan, UT, USA), an infrared forward-scatter sensor that operates at an effective wavelength of approximately 850 nm. The sensor measures light scattering at a 42° sample angle to estimate the meteorological optical range (MOR) with a system accuracy of ±10%. Measurements are recorded at 1 min intervals, and the surface extinction coefficient ($\beta_{ext,sfc}$) is derived using the Koschmieder relation:

$$\beta_{ext,sfc} = \frac{-\ln(0.05)}{\mathrm{MOR}} = \frac{2.995732}{\mathrm{MOR}}, \quad (1)$$

These 1 min observations are averaged into hourly intervals (e.g., the average value at 11:00 LST represents the mean over the period from 11:00 to 12:00 LST). To exclude ambient moisture artifacts, such as fog, precipitation, and extreme hygroscopic growth, data points coinciding with rain/fog codes identified by the CS125 present weather sensor or with relative humidity (RH) exceeding 90% are excluded from the primary aerosol extinction analysis. Hygroscopic growth affects both column-integrated AOD and near-surface aerosol extinction by modifying aerosol particle size and optical properties [24,25]. Therefore, its influence on ASH may be partially canceled out when the relative extinction enhancement is similar throughout the atmospheric column, although vertical differences in RH and aerosol hygroscopicity may introduce residual uncertainty.

Hourly surface PM_{10} and $PM_{2.5}$ mass concentrations (μg m^{-3}) are obtained from the National Ambient Air Quality Information Management System (NAMIS) operated by the Daejeon Metropolitan City Institute of Health and Environment. The collected data are transmitted to the National Institute of Environmental Research (NIER) computing system, where they undergo final validation and statistical processing before being archived in a database. To ensure the reliability of the statistical products, only periods in which at least 75% of valid measurements are available within the target averaging interval are included in the statistical calculations.

2.2.2. Column-Integrated Aerosol Properties and Cloud Screening

Column-integrated aerosol optical and microphysical properties are obtained using a POM-02 sky radiometer (PREDE Co., Ltd., Tokyo, Japan) installed on the roof of the KIER building. The instrument measures direct solar irradiance and the angular distribution of

diffuse sky radiance in 11 spectral channels centered at 315, 340, 380, 400, 500, 675, 870, 940, 1020, 1627, and 2200 nm. The 940 nm channel is affected by water-vapor absorption and is therefore not used for aerosol retrieval, while the ultraviolet and short-wave infrared channels are excluded from the present analysis. The AOD and single scattering albedo (SSA) at 380, 400, 500, 675, 870, and 1020 nm are used in the analysis, whereas AOD at 870 nm (AOD870) is employed for deriving the ASH described in Section 2.3. The AE is obtained from a linear least-squares fit of ln(AOD) against ln(λ) over the 400–870 nm range and is hereafter denoted as $AE_{400–870}$. The two radiometric constants required for the retrieval, the calibration constant corresponding to the extraterrestrial solar irradiance and the solid viewing angle, are determined onsite by the improved Langley plot method and by the solar disk-scan method, respectively, following standard SKYNET practice; the AOD error attributable to improved Langley calibration is approximately 0.003–0.01 at an optical air mass of 2 [26].

Retrievals are performed using the standard SKYRAD.pack inversion algorithm, version 4.2 [26,27]. Quality control and cloud screening of the POM-02 observations follow the multistep algorithm of Khatri and Takamura [28]. Because version 4.2 employs a global flux test as part of its screening procedure, co-located broadband irradiance measurements are required; global solar irradiance recorded by an SMP-10 pyranometer (Kipp & Zonen, Delft, The Netherlands) mounted adjacent to the sky radiometer is therefore incorporated into the screening workflow to detect temporal fluctuations induced by clouds. The procedure additionally combines a spectral variability test [29] with the statistical criteria of Smirnov et al. [30], which require a minimum number of observations per hour and assess diurnal stability, temporal smoothness, and removal of outliers exceeding three standard deviations (3σ). Retrievals for which the residual between measured and simulated sky radiances exceeds the algorithm-defined threshold are rejected. Observations coinciding with rain or fog codes reported by the CS125 present weather sensor or with relative humidity exceeding 90% are also excluded, as described in Section 2.2.1, so that the retained dataset represents cloud-free and comparatively dry conditions.

Under such conditions, the retrieval uncertainty of AOD is estimated to be within $\pm$0.01–0.02. The accuracy of the retrieved SSA is considerably lower at low aerosol loading; SKYNET intercomparison studies have shown that SSA retrievals are reliable only when AOD is sufficiently large, and a threshold of AOD at 500 nm (AOD_{500}) $\geq$ 0.2 is commonly adopted for this purpose [31]. Accordingly, the uncertainty in SSA is estimated to be $\pm$0.03–0.05 for AOD_{500} > 0.2, and only retrievals satisfying this criterion are used in the SSA analysis presented in Sections 3.1 and 4.1. An additional uncertainty of approximately $\pm$0.03 in SSA may arise from the assumed surface albedo and solid viewing angle [32].

The column-integrated aerosol volume size distribution, $v(r) = dV/\mathrm{dln}r$, is retrieved using the same version of SKYRAD.pack. In contrast to parametric approaches that prescribe a fixed functional form such as a multimodal log-normal distribution, SKYRAD.pack applies a nonparametric constrained linear inversion. In the present study, the particle radius spectrum from 0.0110 to 18.19 µm is discretized into 40 logarithmically equally spaced bins, each characterized by its geometric center radius $r_{c,i}$. This is a finer discretization than the default configuration of the distributed package and is adopted to resolve the fine and coarse modes, and their transition in greater detail. The forward problem is formulated as a Fredholm integral equation of the first kind that relates the measured spectral direct irradiance and angular sky radiances to the unknown volume concentration $v(r_{c,i})$ in each bin:

$$I_{sky}(\lambda, \Theta) = \int K(r, \lambda, \Theta, m) v(r) d \ln r \quad (2)$$

where K denotes the scattering kernel computed from Mie theory, Θ is the scattering angle, and m is the complex refractive index. Because the inversion of optical radiances is inherently ill-posed and sensitive to observational noise, version 4.2 adopts a Phillips–Twomey-type constrained solution with a homogeneous smoothing constraint, in which minimization of the second-order derivative is imposed on $v(r)$ to suppress unphysical oscillations in the retrieved spectrum. The retrieval proceeds in four steps [26]: an a priori bimodal log-normal size distribution with mode radii of 0.1 and 2 μm and dispersions of 0.4 and 0.8 is first scaled using forward-scattered radiances at scattering angles $\Theta \leq 30°$; the real part of the complex refractive index is then retrieved from radiances at 20–70°; the modal volumes are revised; and finally, the size distribution and complex refractive index are retrieved from the full angular scan. The last step is iterated until the convergence criterion for the agreement between measured and simulated sky radiances is satisfied.

2.2.3. ERA5 PBLH

PBLH is obtained from ERA5, the fifth-generation atmospheric reanalysis produced by the European Centre for Medium-Range Weather Forecasts (ECMWF), which uses the Integrated Forecasting System (IFS) Cy41r2 on 137 hybrid sigma–pressure model levels extending to 0.01 hPa and provides hourly output at a native horizontal resolution of approximately 31 km [33]. The hourly fields on the regular 0.25° × 0.25° latitude–longitude grid are used here. In ERA5, PBLH is a diagnostic single-level parameter defined as the lowest level at which the bulk Richardson number reaches the critical threshold of 0.25, following the formulation of Vogelezang and Holtslag [34]. The value at the ERA5 grid point nearest to the KIER site is extracted and temporally aligned with the hourly ground-based observations. The parameter is archived in meters and is converted to km for consistency with the ASH defined in Section 2.3.

2.3. ASH and Vertical Structure Analysis

ASH is derived by combining the column-integrated AOD from the POM-02 with the near-surface extinction coefficient obtained from the CS125 sensor. The spectral AOD (AOD_λ) is defined as the vertical integral of the extinction profile $\beta_{ext}(z,\lambda)$ with respect to altitude z:

$$AOD_\lambda = \int_0^\infty \beta_{\text{ext}}(z,\ \lambda)\, dz, \tag{3}$$

Assuming an exponentially decaying or equivalent well-mixed aerosol layer model, the ASH at wavelength λ ($H_{A,\lambda}$) can be expressed as follows:

$$H_{\text{A},\lambda} = \frac{AOD_\lambda}{\beta_{\text{ext, sfc}}(\lambda)}, \tag{4}$$

where $\beta_{ext,sfc}(\lambda)$ is the near-surface extinction coefficient at the corresponding wavelength. Physically, $H_{A,\lambda}$ represents an equivalent vertical length scale linking column-integrated aerosol optical loading to near-surface extinction, and therefore characterizes the effective vertical distribution of aerosols rather than the physical top of an aerosol layer. In the present study, the CS125 provides the near-surface extinction coefficient at an effective wavelength of approximately 850 nm. Because no wavelength-dependent surface extinction measurements are available, AOD_{870} from the POM-02, at the wavelength closest to that of the CS125 measurement, is used to calculate ASH:

$$H_{\text{A},870} = \frac{AOD_{870}}{\beta_{\text{ext, sfc}}} \tag{5}$$

with $\beta_{ext,sfc}$ denoting the extinction coefficient measured at 850 nm using the CS125. The wavelength difference between the CS125 and POM-02 measurements is only 20 nm, and the associated spectral discrepancy is expected to be small under typical aerosol conditions. The effect of the wavelength mismatch between the CS125 extinction measurements at 850 nm and the POM-02 AOD measurements at 870 nm was assessed by interpolating AOD to 850 nm using the observed 675–870 nm Ångström exponent. Across 1211 observations, the mean AOD difference was approximately 0.0040, and the mean observation-wise relative increase in AOD, ASH, and R was 2.74%. The original regime assignments were retained for 96.70% of observations, while the regime-wise decrease in AE and increase in SSA500 remained unchanged in direction. These results indicate a limited influence of the wavelength mismatch on the evaluated relationships and support retaining the original analysis based on measured AOD870. The calculation method and detailed comparisons are provided in Supplementary Section S2 and Tables S2 and S3. Because the CS125 measures extinction at a single wavelength near 850 nm, the ASH derived using AOD_{870} is hereafter denoted simply as H_A, even if it is a function of wavelength in Equation (4).

To compare the aerosol vertical scale with the thermodynamic boundary layer depth, the dimensionless ratio R between H_A and PBLH from the ERA5 dataset is defined as

$$R = \frac{H_{\mathrm{A}}}{\mathrm{PBLH}}, \tag{6}$$

where the ratio R serves as the quantitative criterion for classifying observation periods into three distinct aerosol vertical distribution regimes; (1) surface-concentrated, (2) well-coupled, and (3) column-enhanced/vertically decoupled. Detailed physical interpretations, threshold choices, occurrence frequencies, and atmospheric implications of these three regimes are examined and discussed in subsequent sections.

2.4. Microphysical Particle Size Categorization

The column-integrated volume size distribution (VSD) retrieved from the POM-02 is further analyzed to quantify the contributions of fine- and coarse-mode aerosols. Fine-mode (V_f) and coarse-mode (V_c) volumes ($\mu m^3\ \mu m^{-2}$) are calculated by integrating the distribution over their respective radius domains, separated by the local minimum between 0.4 mm and 0.6 mm:

$$V_f = \int_{r_{\mathrm{min}}}^{r_{\mathrm{inflect}}} \frac{dV}{d\ln r} d\ln r, \tag{7}$$

$$V_c = \int_{r_{\mathrm{inflect}}}^{r_{\mathrm{max}}} \frac{dV}{d\ln r} d\ln r. \tag{8}$$

The coarse-mode volume fraction (CMVF) is then evaluated as follows:

$$\mathrm{CMVF} = \frac{V_c}{V_f + V_c}. \tag{9}$$

These microphysical parameters are evaluated across the identified vertical regimes to distinguish fine-mode-dominated anthropogenic pollution from coarse-mode-dominated mineral dust or sea salt transport events.

3. Results

3.1. Monthly Characteristics of Aerosol Optical Properties

Before examining H_A and aerosol vertical structure, the monthly distributions of AOD_{500}, $AE_{400–870}$, and SSA_{500} are examined to characterize the seasonal background and variability in the observed aerosols. Figure 2a presents the monthly distributions obtained by pooling all quality-assured retrievals during the investigation period from May 2023 to

January 2026. In each panel, the box denotes the interquartile range (IQR), with the median indicated by the horizontal line, and the whiskers extend to 1.5 times the IQR, so that values outside this range are not displayed. The number of hourly retrievals contributing to each month is given at the top of each panel and ranges from 35 in July to 238 in May. No retrieval passes the quality-control and cloud-screening procedures in February, and that month is therefore left blank in Figure 2. Because the record covers 33 months, each calendar month is sampled in only two or three years, and March and April are sampled in only two years. The monthly statistics thus describe the aerosol conditions encountered during this specific period rather than representing a long-term climatology. Since several monthly distributions are asymmetric and exhibit substantial spread, both the median and the IQR are used to describe the monthly variability.

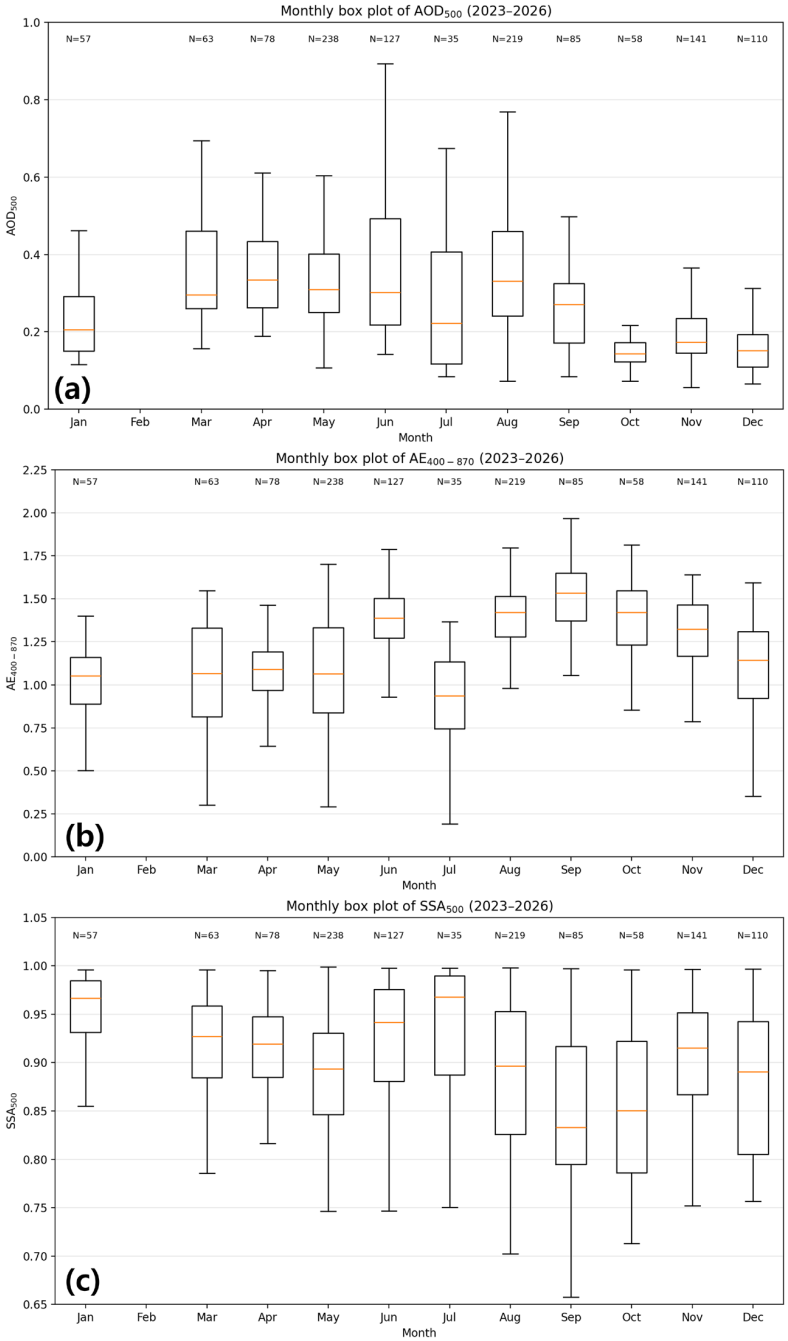


Figure 2. Monthly distributions of aerosol optical properties during 2023–2026: (**a**) AOD_{500}, (**b**) $AE_{400–870}$, and (**c**) SSA_{500}. The number of observations for each month is shown at the top of each panel.

AOD_{500} shows clear seasonal differences in both its magnitude and variability. The median value of AOD_{500} increases from 0.21 in January (IQR: 0.15–0.29) to 0.30–0.33 during March–June, with an annual maximum of 0.33 in April, and remains comparably high in August (0.33; IQR: 0.24–0.46). The distributions during spring and summer are generally wide. For example, the IQR extends from 0.26 to 0.46 in March and from 0.22 to 0.49 in June, indicating that enhanced aerosol loading during these periods is accompanied by substantial short-term variability. July interrupts this pattern, with the lowest summer median of 0.22 and a wide IQR of 0.12–0.41, which is consistent with efficient wet removal during the summer monsoon rain band, although only 35 retrievals are available for that month. In contrast, AOD500 decreases during autumn and early winter, with median values of 0.27, 0.14, 0.17, and 0.15 for September, October, November, and December, respectively. The October distribution is particularly narrow (IQR: 0.12–0.17), indicating relatively persistent low aerosol concentrations compared with spring and summer. The standard deviation shows a similar seasonal contrast, reaching approximately 0.15–0.20 from March to August but declining to approximately 0.08–0.10 during October–December.

The seasonal behavior of AOD_{500} is broadly consistent with previous ground-based observations over Korea and East Asia, although the timing of the reported maximum varies. Kim et al. [4] found that the seasonal average of aerosol optical thickness at East Asian sky radiometer sites, including the Korean sites of Anmyon and Gosan, generally exhibits a maximum in spring and a minimum in autumn. Studies that included the summer months over Korea, in contrast, reported a maximum in early summer or summer. Eck et al. [35] described a spring and/or summer maximum and a winter minimum at AERONET sites in China, Mongolia, Korea, and Japan, and Eck et al. [36] showed that the monthly mean fine mode AOD_{500} nearly doubles from May to June at Anmyon, coinciding with multiyear increases in cloud fraction and relative humidity and a reduction in wind speed. From AERONET measurements at ten Korean sites, Zhai et al. [10] reported that AOD over South Korea has a summer maximum and a winter minimum, with a weaker amplitude than that observed over North China, and that transport from the Asian continent is strongest in spring. The distributions in Figure 2a, which combine comparable medians in spring and August with a distinct minimum in autumn and early winter, are consistent with this description, whereas the low July values indicate that the summer maximum at the present site is interrupted by monsoon precipitation.

Figure 2b presents the monthly variability of $AE_{400–870}$, which exhibits a seasonal behavior distinct from that of AOD_{500}. Median $AE_{400–870}$ values remain approximately 1.05–1.09 during January, March, April, and May, while the distributions during several spring months are relatively wide. In March, for example, the median is 1.07 with an IQR of 0.81–1.33, and May shows a similarly wide IQR of 0.84–1.33. AE400–870 increases to 1.39 in June, falls temporarily to 0.94 in July, and subsequently increases to 1.42 in August and 1.53 in September. The September distribution is relatively concentrated (IQR: 1.37–1.65), suggesting that the high AE400–870 values represent a persistent monthly characteristic rather than reflecting the effect of a small number of extreme observations. Elevated AE400–870 values persist through October (1.42) and November (1.32) before the median falls to 1.14 in December.

The relatively low and widely distributed AE400–870 values observed during parts of spring are consistent with variable contributions from coarse-mode aerosols. Eck et al. [35] found a springtime minimum in the AE at East Asian AERONET sites associated with dust storm activity, while noting that the monthly mean value between 440 and 870 nm remains above 0.8 even during the peak dust season. Shin et al. [37] showed that dust-containing aerosol types accounts for as much as 82% of the cases at Gosan in April, with type-mean AEs ranging from 0.17 for pure dust to 1.36 for pollution. The higher and

relatively more concentrated AE400–870 values observed during late summer and early autumn suggest a more persistent contribution from fine mode particles. This behavior agrees with Jung et al. [38], who obtained the highest seasonal AE in autumn from POM-02 measurements in Seoul and attributed it to freshly emitted fine mode particles, such as those from post-harvest biomass burning, and with Noh et al. [39], who reported the highest AEs of 1.43 ± 0.30 at Gwangju and 1.49 ± 0.20 at Anmyon.

The low median in July requires careful interpretation because this month combines the lowest AOD_{500} of the record with the smallest number of retrievals. At low aerosol loading, the AE becomes numerically unstable; for optical thicknesses of about 0.05 and 0.02 at 500 and 865 nm, absolute AOD differences of 0.01 and 0.005 can produce AE differences of up to approximately one [26]. In addition, the AE is not a unique measure of particle size, since it responds to the volume fraction of particles with radii smaller than about 0.6 μm rather than the fine-mode effective radius [40], and it decouples from the fine-mode fraction during the humid Korean summer, when hygroscopic growth and cloud processing increase the size of the fine mode [41]. Eck et al. [36] demonstrated using Mie calculations that a cloud-processed fine mode with a volume median radius of 0.44 μm yields an AE between 440 and 870 nm of only 0.26, compared with 1.52 for a humidified mode of 0.25 μm. A lower AE during the monsoon season therefore does not necessarily indicate the presence of dust.

Considerable seasonal variability is also found in SSA_{500} in Figure 2c, with its monthly behavior following neither AOD_{500} nor $AE_{400–870}$. Relatively high median SSA_{500} values occur in January (0.97; IQR: 0.93–0.98), July (0.97; IQR: 0.89–0.99), June (0.94; IQR: 0.88–0.98), and March (0.93; IQR: 0.88–0.96). In contrast, the lowest median SSA_{500} values occur in September (0.83) and October (0.85), and comparatively low values are also found in May (0.89) and August (0.90). The spread of the SSA_{500} distributions varies markedly among months. The distribution is narrowest in January, with a standard deviation of 0.05, whereas substantially wider distributions occur during late summer and autumn, with standard deviations of approximately 0.075–0.078, indicating greater temporal variability in the aerosol scattering and absorption characteristics during these periods.

The interpretation of the monthly SSA_{500} variability requires explicit consideration of the retrieval sensitivity because the accuracy of SSA decreases rapidly as the aerosol loading decreases. AERONET restricted its quality-assured SSA product to cases with AOD at 440 nm greater than 0.4 [42,43], and Dubovik et al. [44] noted that the characterization of low-optical-depth situations is the principal limitation of such retrievals, since an absolute AOD error of ±0.01 already implies a relative error of 20% or more. Mok et al. [45] found that relaxing the criterion to an AOD at 440 nm greater than 0.2 in Seoul lowers the mean SSA by approximately 0.02 relative to the restricted sample, and that an overestimation of AOD translates into an underestimation of SSA. At the present site, the median AOD_{500} is lower than 0.2 in October, November, and December and is close to 0.2 in January, meaning that a large fraction of the cold-season retrievals lies below the loading for which SSA is well constrained. The high and narrowly distributed SSA_{500} values in January are therefore not interpreted as evidence of exceptionally weak absorption, particularly because independent measurements in Korea indicated the opposite tendency during the cold season. The concentrations of brown carbon and water-soluble organic carbon in Seoul decreased by approximately 80% and 30%, respectively, from the cold season to the warm season [46]; the columnar black carbon amount increased in spring and winter because of heating and long-range transport and decreased in summer through wet scavenging [47]; and the carbonaceous aerosol fraction reached 13.8% in winter but remained below 2% in summer [48]. The SSA_{500} values obtained during the higher-loading months are consequently more robust, and the September minimum, which coincides with

the highest $AE_{400–870}$ in the record, indicates a fine and comparatively absorbing aerosol population in early autumn, whereas the similar October value is accompanied by a median AOD_{500} of 0.14 and is therefore subject to greater uncertainty.

The combined seasonal variations in AOD_{500}, SSA_{500}, and $AE_{400–870}$ provide additional constraints on the dominant aerosol characteristics. Relatively low $AE_{400–870}$ values accompanied by enhanced AOD_{500} generally indicate an increased contribution from coarse-mode particles, which is consistent with mineral dust or other mechanically generated aerosol. This feature is particularly relevant during spring in Korea, when Asian dust transport frequently enhances the coarse-mode fraction and reduces the columnar AE. From AERONET observations in South Korea, Zhai et al. [10] found that the total AOD in spring, ranging from 0.4 to 0.6, is twice as large as the fine-mode AOD of 0.2 to 0.3, reflecting a large contribution from dust, whereas in the other seasons 80–90% of the total AOD is contributed by the fine mode. Similarly, Eck et al. [36] found that the increase in total AOD from May to June is smaller than that in fine-mode AOD because of the larger coarse-mode AOD during the spring months. It should be noted, however, that the coarse-mode AOD provided by such retrievals tends to overestimate the mineral dust contribution [37].

Higher $AE_{400–870}$ values during late summer and autumn generally indicate a greater relative contribution from fine-mode particles. The interpretation of SSA, however, requires caution because SSA depends not only on particle size but also on chemical composition, relative humidity, internal or external mixing, and the absorbing properties of dust and carbonaceous aerosol. In particular, Asian dust exhibits variable SSA depending on its mineralogical composition and mixing state. Kim et al. [4] reported an SSA of approximately 0.9 for dust particles over East Asia at 500 nm, with lower values when dust is mixed with anthropogenic aerosol from the Asian continent, and Noh et al. [39] obtained the lowest column-mean SSA at 440 nm of 0.89 ± 0.02 at Gwangju and 0.88 ± 0.02 at Anmyon during dust advection. Under humid and cloudy conditions, in contrast, AERONET retrievals and airborne in situ measurements over Korea both showed high SSA together with substantial enhancements in AOD at ambient relative humidity [49]. The combination of high AE and low SSA may therefore suggest fine-mode aerosol with a stronger absorbing component, but it should not be regarded as a unique source diagnostic. The frequency distributions of the absorption AE overlapped substantially among aerosol types, and the distributions of urban or industrial aerosol and of biomass-burning aerosol were nearly identical for values above 1.0 [50]. The classification of Korean observations also varied with the parameter thresholds adopted [48] and differed among classification methods [51]. AOD, AE, and SSA are thus more appropriately used to infer broad changes in aerosol size and radiative properties than to attribute individual observations to specific source types.

3.2. Monthly Characteristics of ASH

Figure 3 shows the monthly median values of H_A along with PBLH during the observation period. Valid monthly statistics are obtained for 23 of the 33 calendar months of the record; October 2023 to February 2024, January and February 2025, and May to July 2025 contain no retrieval that passes quality–control criteria, and these gaps appear as breaks in Figure 3. The number of coincident hourly pairs per month ranges from 2 in July 2023 and September 2025 to 128 in May 2024; therefore, months represented by fewer than approximately 15 pairs are regarded as indicative rather than representative. It should also be noted that the PBLH medians shown in Figure 3 are evaluated at exactly the hours for which a valid H_A is available, that is, during cloud-free daylight hours. They are therefore directly comparable with H_A, but they do not represent the full diurnal cycle of the boundary layer, which includes the shallow nocturnal layer. Both H_A and PBLH exhibit pronounced month-to-month variability, and their relationship varies considerably over

time. Such differences are physically plausible because both AOD and ASH depend not only on the depth of the meteorological boundary layer but also on aerosol type, vertical transport, relative humidity, particle size, and the presence of elevated aerosol layers. In airborne observations over South Korea during the KORUS-AQ campaign, 76–90% of the column aerosol extinction was found within the 0–2 km layer and 9–19% within the lower free troposphere between 2 and 5 km, whereas only 58% of the column aerosol mass was located below 2 km and 34% between 2 and 5 km, where dust dominated the mass [10]. The vertical distribution of aerosol optical extinction can therefore differ substantially from that of aerosol mass and from the diagnosed meteorological boundary layer.

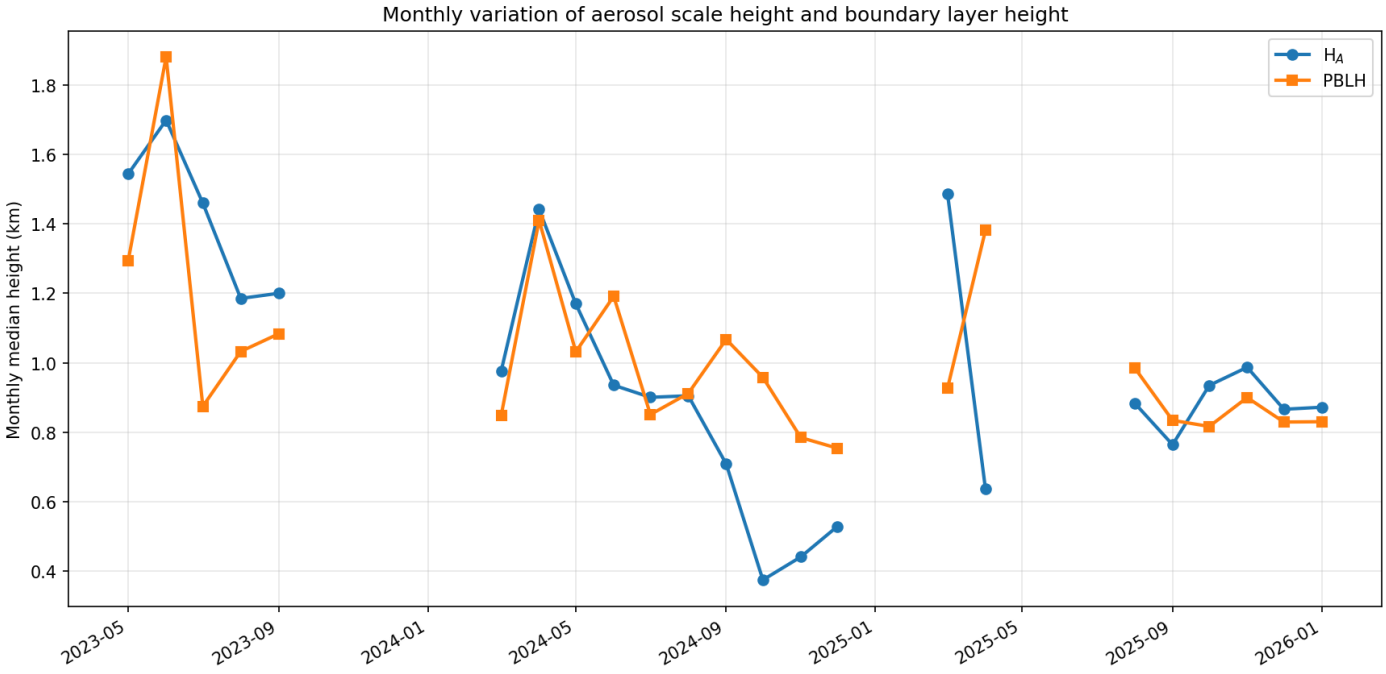


Figure 3. Monthly variation in the median values of H_A (blue line with circles) and ERA5 PBLH (orange line with squares) during the observation period. Missing months indicate periods for which no valid observations were available.

During May–September 2023, H_A generally remains above 1 km, with monthly median values ranging from 1.19 to 1.70 km. The highest monthly median H_A occurs in June 2023 (1.70 km), when the corresponding PBLH is also the highest recorded value, at 1.88 km, although this month is represented by only 14 pairs. The concurrent increases in H_A and PBLH in June may reflect stronger turbulent mixing and more efficient vertical redistribution of aerosol within the lower troposphere. Cheng et al. [16] examined a similar coupling between aerosol vertical structure and boundary-layer development over East Asia using spaceborne lidar and found that the extinction peak of polluted continental aerosol occurs at approximately 1 km and shifts with changes in boundary-layer height, so that the seasonal and diurnal variation in the extinction profiles is closely associated with changes in PBLH. In contrast, H_A (1.46 km) is substantially higher than PBLH (0.87 km) in July 2023. Because only two valid observations are available for that month, this contrast is not interpreted as a monthly characteristic; it is nevertheless consistent with the possible influence of aerosol above the meteorological boundary layer, such as transported dust or other elevated layers. Aerosol scale-height retrievals over Gwangju, Korea, similarly showed that elevated dust above the boundary layer can produce substantial differences between the retrieved aerosol vertical profile and the lidar-derived profile, with derived scaling heights spanning 0.39 to 3.55 km [19].

In 2024, H_A and PBLH show relatively similar values during spring and summer. For example, the monthly median H_A and PBLH in April are 1.44 and 1.41 km, respectively, and in August the corresponding values are 0.90 and 0.91 km, with the latter month represented by 125 pairs. These periods of close agreement suggest that the aerosol optical extinction is predominantly confined to the meteorological boundary layer. This interpretation is consistent with the aircraft observations over South Korea reported by Zhai et al. [10], which showed that the optically dominant sulfate–nitrate–ammonium and organic aerosol are mainly confined to the boundary layer, even though dust contributes appreciably to the aerosol mass of the lower free troposphere. A clear divergence emerges from September to December 2024. During this period, H_A decreases from 0.71 km in September to a minimum of 0.37 km in October and remains relatively low in November and December, with median values of 0.44 and 0.53 km, respectively. The corresponding PBLH values are consistently higher, with values ranging from approximately 0.75 to 1.07 km. The October minimum is well constrained, as its interquartile range spans only from 0.30 to 0.45 km over 30 pairs, indicating that the shallow effective aerosol vertical extent of that month is a robust feature rather than the effect of individual outliers. The effective aerosol vertical extent during autumn and early winter 2024 is thus substantially smaller than the diagnosed meteorological boundary–layer depth. A lower H_A than PBLH can occur when aerosol extinction is concentrated near the surface because of stable stratification, weak vertical mixing, aerosol removal, or a vertically inhomogeneous aerosol distribution. Su et al. [17] classified such profiles as the decreasing type, in which the extinction coefficient peaks at the surface and declines with increasing height within the boundary layer, in contrast to well-mixed and inverse profiles. Over North China, the aerosol extinction coefficients declined rapidly with altitude below approximately 2 km, while the peak altitude of polluted continental aerosol varied with the boundary-layer height [16]. In addition, observations over Korea showed that transported plumes above a shallow nocturnal boundary layer are entrained downward as the mixed layer deepens during the day, indicating that the vertical distribution of pollutants is strongly modulated by diurnal changes in atmospheric structure [52]. Surface measurements in South Korea likewise indicated that $PM_{2.5}$ is highest during the colder months from October to March under shallow mixing depths and stagnant conditions, whereas AOD peaks from March to August [53]. The autumn and early winter 2024 reduction in H_A may therefore reflect a strong near-surface concentration of optically active aerosol within only part of the meteorological boundary layer.

This episode, however, is not observed again in the following year. From October to December 2025, H_A remains between 0.87 and 0.99 km and slightly exceeds the corresponding PBLH values of 0.82 to 0.90 km, in contrast to the ratio of approximately 0.4 to 0.7 obtained for the same months of 2024. Because the autumn and early winter of 2023 are missing from the record, only two years of observations for this season are available, and they differ qualitatively. The pronounced autumn minimum of H_A is consequently interpreted as a feature of the specific conditions prevailing in late 2024 rather than as an established seasonal characteristic of the site, and the seasonal statistics presented in Section 3.3 are correspondingly influenced by that single year of observations.

A contrasting pattern is observed in March 2025, when the monthly median H_A reaches 1.49 km, whereas the PBLH remains at 0.93 km, although this month is represented by only 13 pairs. The elevated ASH may be associated with transported dust or other elevated aerosol layers, which are particularly relevant during the spring dust season in Korea. During KORUS-AQ, dust was found to contribute substantially to the aerosol mass of the lower free troposphere, while fine anthropogenic aerosol within the boundary layer dominated the aerosol extinction [10]. Consequently, an H_A larger than PBLH does not imply that the entire aerosol layer is uniformly mixed throughout the free troposphere;

rather, it may indicate the presence of an optically significant elevated layer. Previous observations at Gwangju also showed that aerosol scaling heights were considerably larger under dust-dominant conditions, owing to aerosol layers elevated above the boundary layer [19].

In April 2025, in contrast, the relationship is reversed, with H_A decreasing to 0.64 km while PBLH increases to 1.38 km. The increase in meteorological mixing depth therefore does not result in a proportionate increase in aerosol vertical extent. Such behavior can occur when aerosol loading is concentrated in the lower part of the boundary layer, when aerosol concentrations are reduced at higher altitudes, or when removal processes offset the effect of enhanced turbulent mixing. The distinction between aerosol mass and aerosol optical extinction is important in this regard: over South Korea, the aerosol extinction was more strongly weighted toward the boundary layer than the aerosol mass because fine, hygroscopic aerosol within the boundary layer had a higher mass extinction efficiency than coarse dust in the free troposphere [10]. From August 2025 to January 2026, both quantities become more comparable, generally remaining within approximately 0.8 to 1.0 km, except in September 2025, when only two valid observations are available. The close correspondence during this period suggests that the dominant aerosol optical loading is largely confined to or closely associated with the meteorological boundary layer. The limited number of valid observations in September 2025 nevertheless introduces considerable uncertainty; the corresponding monthly relationship is therefore interpreted with caution.

Finally, part of the month-to-month difference between H_A and PBLH may reflect uncertainty in the reanalysis boundary-layer height itself. A comparison of the ECMWF reanalysis boundary-layer height with lidar-derived values at 20 AD-Net sites over East Asia indicated that the reanalysis is generally lower than the lidar-derived estimate, with mean differences of approximately -0.64 km in summer and -1.09 km in winter at inland sites [22]. The months in which H_A falls well below PBLH, such as October to December 2024, are therefore not explained by this uncertainty alone, since a deeper true boundary layer would further increase the discrepancy. Conversely, part of the excess of H_A over PBLH observed in July 2023 and March 2025 may arise from an underestimated reanalysis boundary-layer height, and differences of a few hundred meters between the two quantities may therefore fall within the range of this uncertainty. For this reason, the subsequent analysis is based on the ratio of H_A to PBLH, grouped into broad regimes, rather than on the exact difference between the two heights.

3.3. Seasonal Characteristics of Aerosol Vertical Structure

The seasonal variation in aerosol vertical structure is examined to assess differences in the relationship between H_A and PBLH. Figure 4 shows the seasonal distribution of R, with the dashed horizontal line representing R = 1. The seasonal distributions exhibit clear differences in both the median and variability of R. The median R is highest in spring (1.15), followed by summer (1.03), winter (0.91), and autumn (0.78). Spring is characterized not only by the highest median R but also by the broadest upper range, indicating a greater frequency of conditions in which H_A exceeds PBLH. This seasonal feature is consistent with previous observations over Korea and East Asia that show enhanced aerosol loading and more complex aerosol structures during spring [4]. Long-term ground-based sky-radiometer measurements over East Asia have shown that aerosol optical thickness generally reaches a seasonal maximum in spring, partly because of the frequent influence of Asian dust and transported aerosol plumes [4]. Multi-year satellite, lidar, and Sun/sky radiometer observations have also shown enhanced aerosol extinction in the middle troposphere during spring, whereas aerosol loading tends to decrease during autumn and winter [6]. The relatively large springtime values of R are particularly relevant

to the aerosol vertical structure over the Korean Peninsula. Lidar observations in Seoul have demonstrated that Asian dust transported from northern China and Mongolia formed elevated aerosol layers during transport to Korea, contributing substantially to column aerosol loading even when the aerosol distribution near the surface does not fully represent the entire atmospheric column [54]. Similarly, a scaling-height analysis performed at Gwangju, Korea, showed that discrepancies between aerosol scaling height and lidar-derived aerosol vertical profiles were largest under dust-dominant conditions, which were attributed to uplifted dust layers above the PBL [19]. These previous findings support the interpretation that R > 1 may occur when a significant fraction of aerosol extinction is located above or weakly coupled to the near-surface mixed layer.

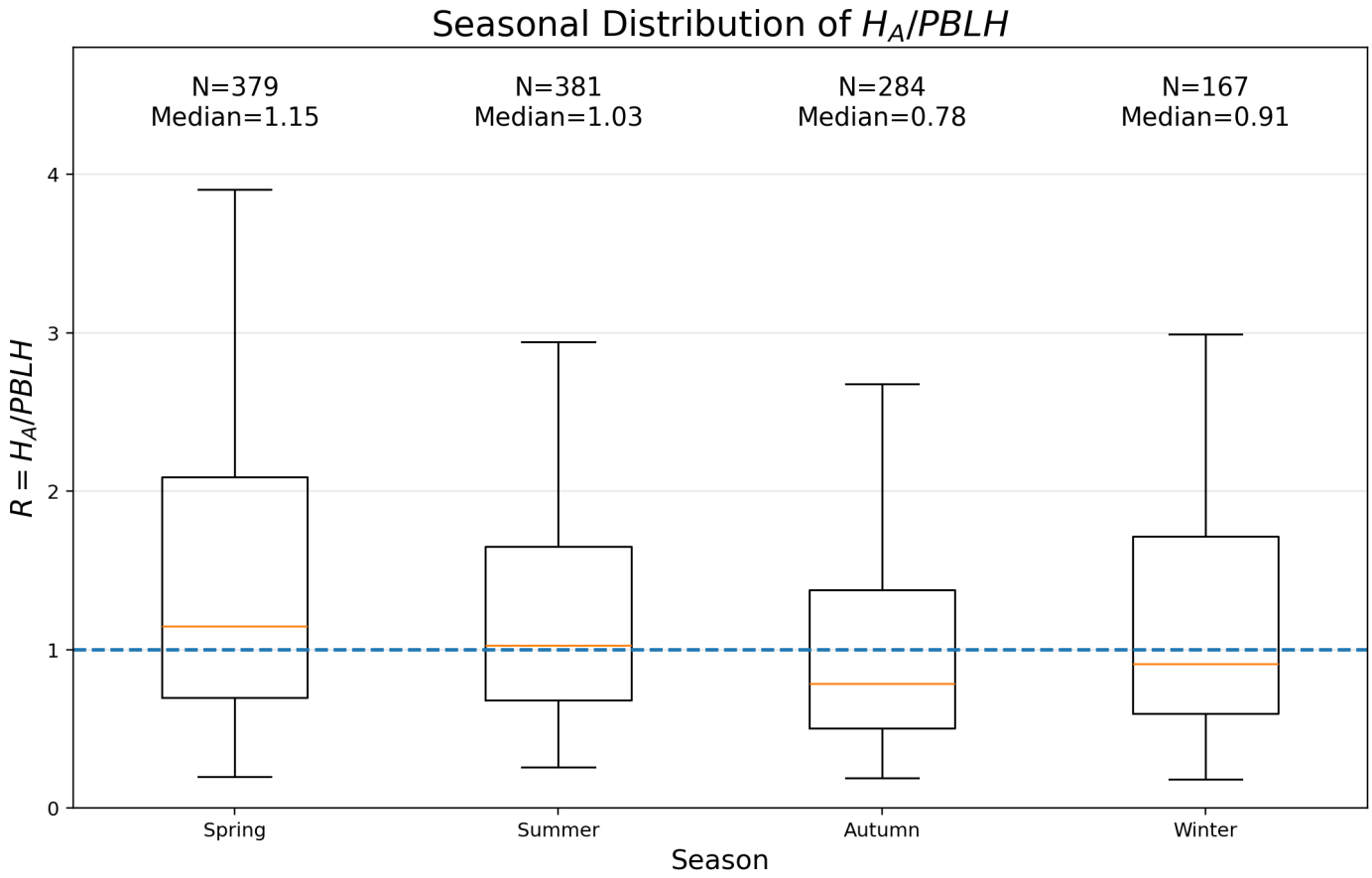


Figure 4. Seasonal distributions of *R*. The dashed horizontal line marks R = 1, corresponding to equal aerosol scale height and planetary boundary layer height. The number of observations (N) and seasonal median values are indicated above each boxplot.

The broader East Asian climatology also indicated that dust and mixed dust–pollution aerosol are frequently present above the local boundary layer. CALIPSO-based analyses have identified a dust transport belt extending from the Taklimakan and Gobi Deserts across eastern China toward Korea, Japan, and the northwestern Pacific. Dust occurrence was generally most frequent in spring, and dust layers were able to extend several kilometers above the surface, although their vertical extent and extinction structure change substantially between source and downwind regions [55]. Long-term CALIPSO observations further showed that dust, polluted dust, and smoke transported over long distances contribute substantially to aerosol loading over East Asia; pure dust transport is especially evident along downwind transport pathways in winter and spring [11]. Aircraft and lidar observations have also documented seasonal variations in free-tropospheric aerosol transport over East Asia [56].

Summer shows a median R of 1.03, close to the reference value of unity, suggesting that H_A and PBLH are generally similar in magnitude during this season. Such correspondence is consistent with conditions in which near-surface extinction more closely represents the aerosol loading distributed throughout the meteorological boundary layer. However, summer still exhibits a substantial upper range of R, indicating that aerosol vertical structure is not uniformly coupled under all conditions. Previous studies over East Asia have shown that summer aerosol loading can also be enhanced by stagnant synoptic conditions, secondary aerosol formation, hygroscopic growth under high relative humidity, and regional transport, particularly across the Korean Peninsula and adjacent regions [6].

In contrast, autumn exhibits the lowest median value of R, at 0.78. Values of $R < 1$ indicate that the column-integrated AOD can be explained by a vertical extent smaller than the diagnosed PBLH under the assumption that the observed near-surface extinction coefficient is vertically uniform. This condition is therefore consistent with aerosol extinction being preferentially concentrated within the lower portion of the boundary layer rather than being uniformly distributed throughout its full depth. The relatively low autumn R is also consistent with previous East Asian observations of generally lower column aerosol loading during autumn compared with spring [4,6]. Winter has a median R of 0.91, slightly below unity, but its relatively broad distribution indicates substantial case-to-case variability. This variability may reflect alternating conditions characterized by shallow near-surface aerosol accumulation and elevated or long-range transported aerosol layers. Observations over South Korea have shown that transboundary aerosol plumes can initially arrive above a shallow nocturnal boundary layer and subsequently be mixed downward as the daytime boundary layer develops, demonstrating that the relationship between surface aerosol concentrations and column aerosol loading can vary substantially with atmospheric vertical structure [52]. These seasonal differences in R values are further examined in the discussion in relation to aerosol optical and microphysical characteristics.

4. Discussion

4.1. Aerosol Optical Characteristics Based on ASH

The relationship between aerosol vertical structure and particle-size characteristics is first examined using $AE_{400–870}$ across different R ranges (Figure 5a). The median $AE_{400–870}$ remains approximately 1.41 for $R < 0.75$ and decreases progressively with increasing R, reaching approximately 1.00 at R = 3.0–5.0. Although a slight increase is observed for $R > 5.0$, the overall decrease in $AE_{400–870}$ indicates a systematic shift toward larger particle sizes with increasing divergence between ASH and PBLH. This interpretation is consistent with observations over Korea and East Asia showing that lower AE is associated with an increasing contribution from coarse-mode aerosols. Multi-year sun–sky radiometer observations at Gosan and Anmyon showed substantially lower AE during Asian dust periods than during non-dust spring conditions, while regional observations across East Asia similarly reported lower AE and enhanced coarse-mode contributions under dust-influenced conditions [57,58]. Airborne measurements during KORUS-AQ further demonstrated that elevated aerosol layers over Korea can exhibit flatter AOD spectra and lower AE than aerosol in the lower atmosphere, reflecting a greater coarse-mode contribution at altitude [21]. The relationship becomes clearer when the median R and $AE_{400–870}$ values of each interval are compared on a logarithmic R scale (Figure 5b), with $\gamma^2 = 0.824$. This result indicates that increasing divergence between H_A and PBLH is accompanied by systematic changes in column aerosol size characteristics. Previous studies have shown that aerosol scaling height derived from column optical depth and surface extinction varies substantially under different atmospheric conditions, including pronounced seasonal variability

over East Asia [18]. However, the dependence of such scaling-height departures on column aerosol size characteristics has received relatively little attention.

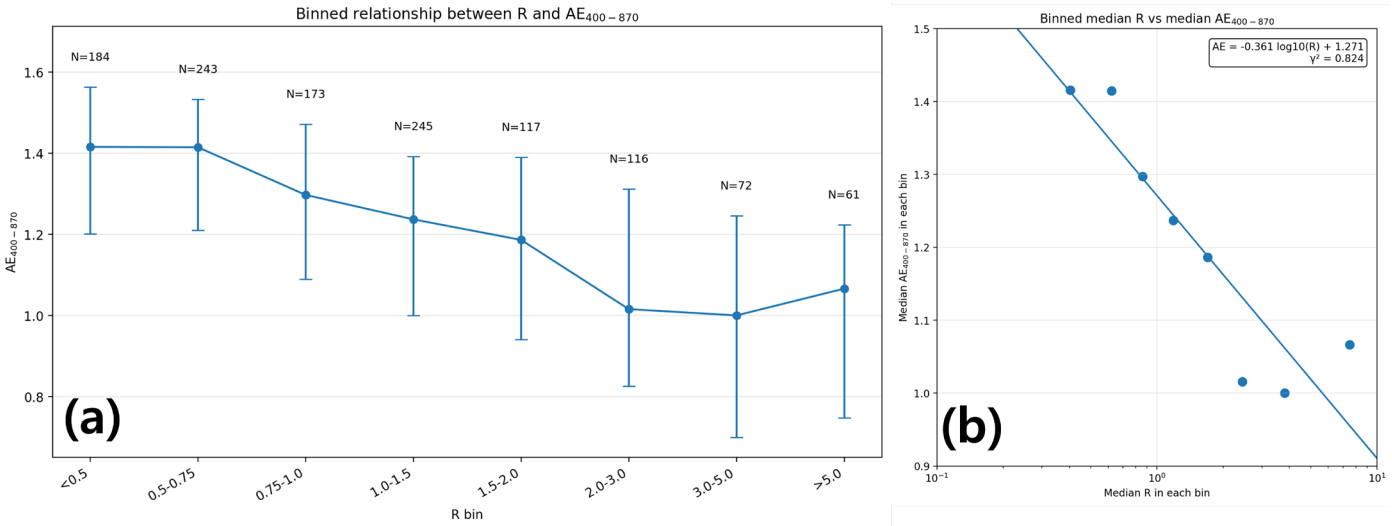


Figure 5. Distribution (**a**) and scatter plot (**b**) of $AE_{400–870}$ for binned R during the investigation period. In (**b**), the *x*-axis is on a logarithmic scale.

The columnar VSD provides direct microphysical support for the particle-size shift inferred from AE (Figure 6). For R < 1, the distributions exhibit a pronounced fine-mode peak at approximately 0.1–0.2 μm and a comparatively modest coarse-mode contribution. As R increases above 1, the coarse-mode contribution progressively increases, particularly at radii of several micrometers, while changes in the fine-mode peak are comparatively limited. Similar coarse-mode enhancements have been reported in sun–sky radiometer observations of Asian dust transported to Korea. Yu et al. [57] identified coarse-mode radii of approximately 1.3–3.8 μm in East Asian dust, including at downwind sites in Korea and Japan, while long-term observations at Gosan and Anmyon showed pronounced changes in column aerosol size distributions during Asian dust periods [58]. To quantify this shift, the fine and coarse modes are separated at the minimum in the overall median VSD, corresponding to a radius of 0.595 μm (Figure A1). The median CMVF remains close to 0.50 for R < 1 but increases progressively to 0.55, 0.58, and 0.63 for R = 1.0–1.5, 1.5–2.0, and 2.0–3.0, respectively, and approaches approximately 0.68 for R > 3 (Figure 7a). The bin-level regression further shows a strong positive association between CMVF and $\log_{10}$(R), with γ^2 = 0.889 (Figure 7b). The agreement between the AE and VSD results is physically consistent with previous remote-sensing findings that lower AE was associated with a larger relative contribution from coarse particles. KORUS-AQ observations over Korea likewise showed that coarse-mode aerosol increasingly influences the spectral dependence of columnar AOD when elevated aerosol layers contribute to the total column [21].

The relative changes in V_f and V_c help clarify the origin of the increase in CMVF (Figure 8a). Relative to the R < 0.5 reference group, normalized median V_f increases to approximately 1.5 by R = 1.0–1.5 and subsequently changes little over R = 1.5–5.0. In contrast, V_c increases almost continuously, reaching 3.66 at R = 3.0–5.0 and approximately 3.97 for R > 5. Thus, the increasing coarse-mode fraction at high R primarily reflects an increase in columnar coarse-mode aerosol volume rather than a decrease in fine=mode volume. This behavior is qualitatively consistent with aircraft observations over Korea, where enhanced particle volume at radii above approximately 1 μm was associated with dust influence, and coarse aerosol was present in elevated portions of the atmospheric column [21].

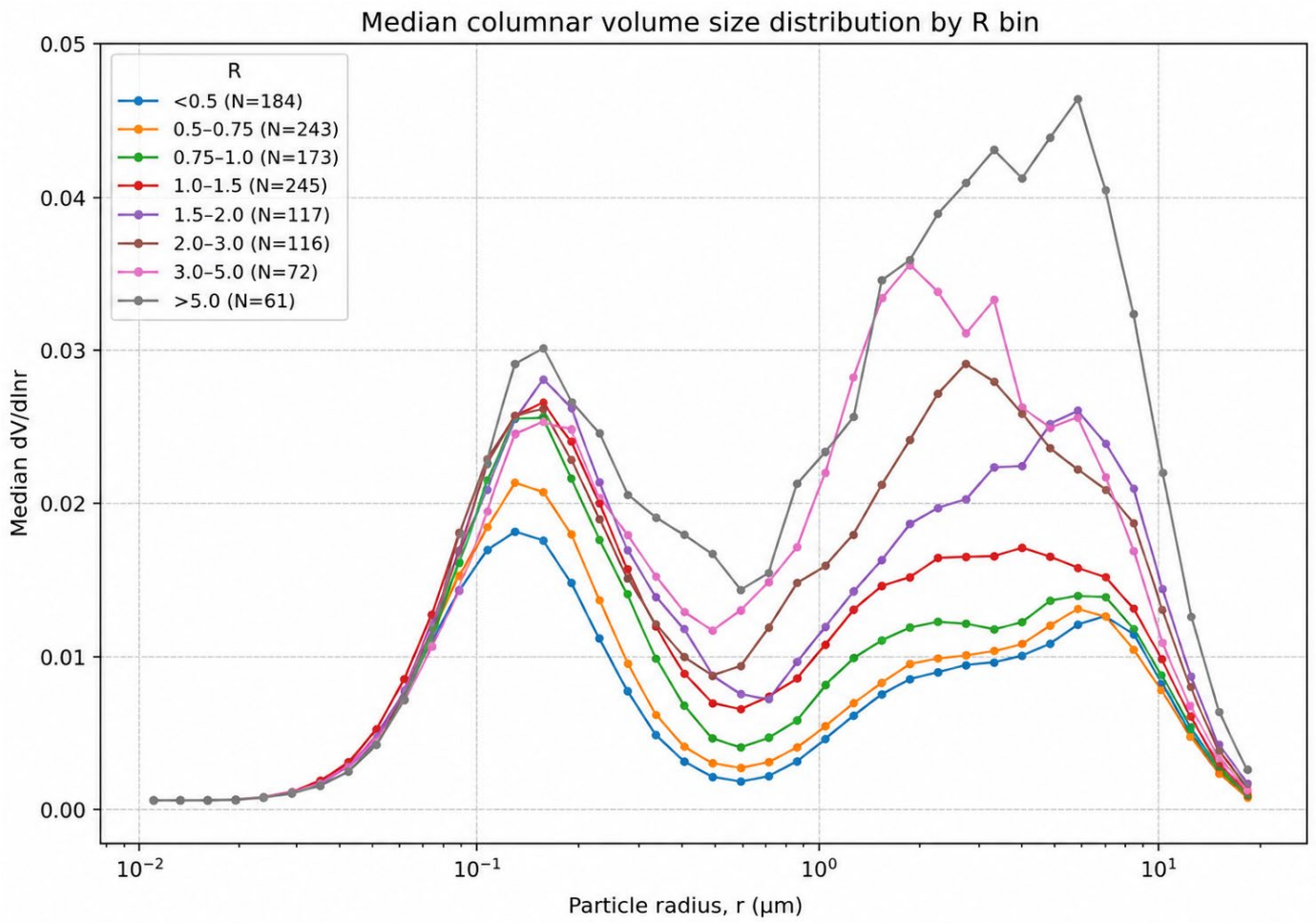


Figure 6. Median columnar volume size distributions for each R bin during the investigation period.

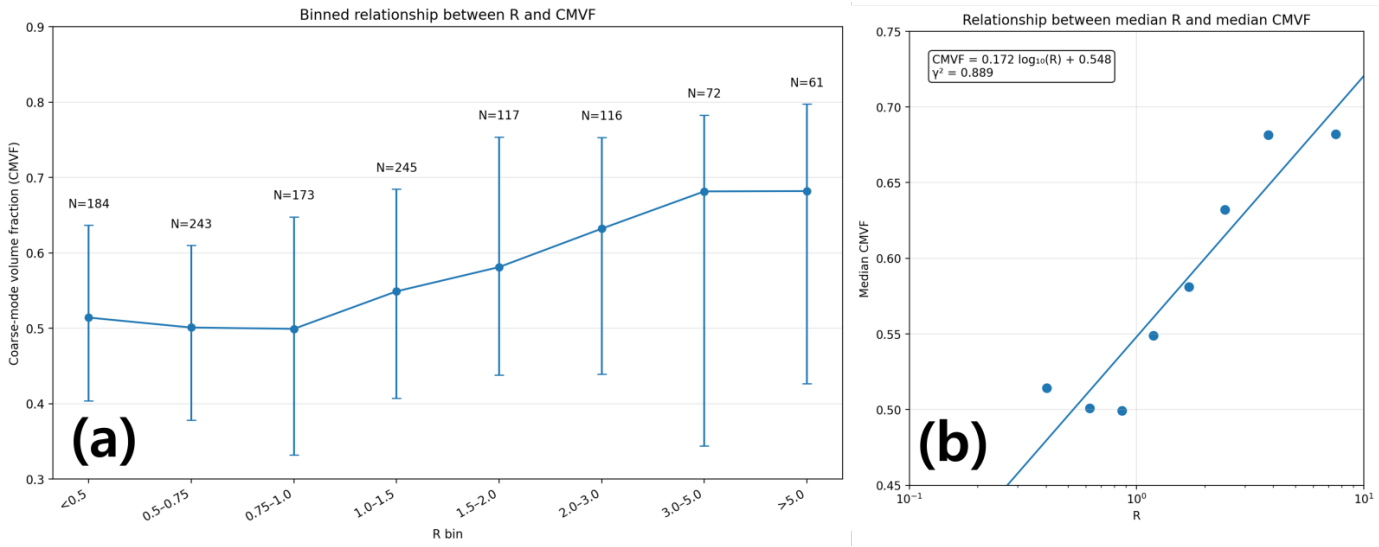


Figure 7. Same as Figure 5 except for CMVF. Distribution (**a**) and scatter plot (**b**) of $AE_{400–870}$ for binned R during the investigation period. In (**b**), the *x*-axis is on a logarithmic scale.

https://doi.org/10.3390/rs18213640

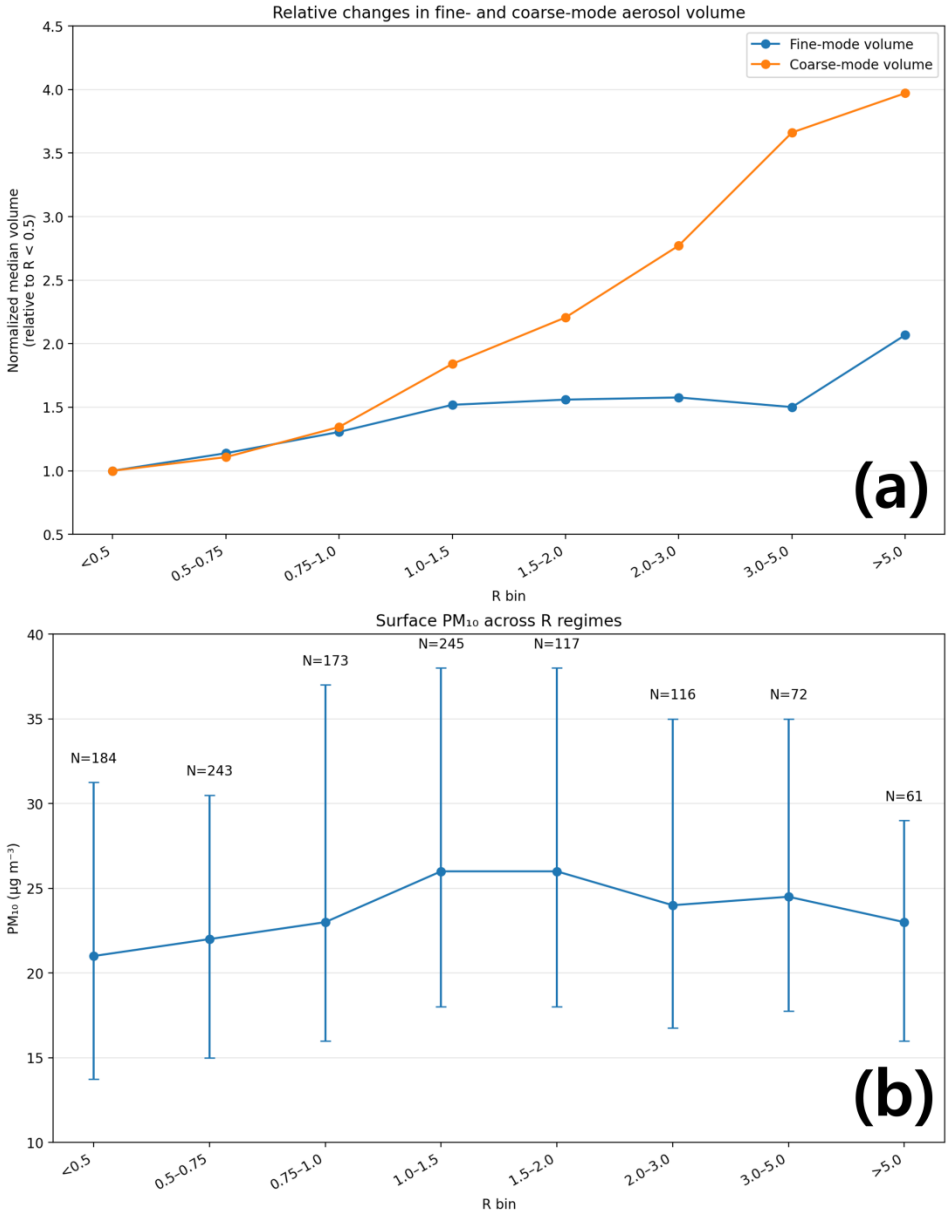


Figure 8. Relative changes in fine- and coarse-mode aerosol volume normalized to the R < 0.5 regime (**a**), and median surface PM_{10} concentrations across each corresponding R bin (**b**) during the investigation period.

In contrast to the pronounced variation in columnar V_c, surface PM_{10} shows little systematic variation with R (Figure 8b). Median PM_{10} increases only modestly from 21 μg m^{-3} at R < 0.5 to 26 μg m^{-3} at R = 1.0–2.0 and then remains within approximately 23–25 μg m^{-3}. The weak relationship is also supported by the individual observations (ρ = 0.08) and the regression based on interval medians (γ^2 = 0.166; Figure A2). This contrast between column-integrated and surface measurements is consistent with observations during KORUS-AQ, which frequently documented vertically stratified aerosol layers over Korea. Peterson et al. [20] reported complex aerosol layering associated with changing meteorological conditions, while aircraft observations showed that transported aerosol could produce elevated aerosol peaks at approximately 1–3.5 km that were not necessarily represented by ground-level aerosol characteristics [59]. The different responses of columnar coarse-mode volume and surface PM_{10} therefore indicate progressively weaker surface–column correspondence at high R. This interpretation is particularly consistent with KORUS-AQ observations showing that lower atmospheric layers over Korea were

generally dominated by fine-mode aerosol, whereas elevated layers could contain relatively coarse transported aerosol [21]. Lidar and aircraft observations have also documented dust layers extending several kilometers above the surface over Korea, with dust extinction observed between approximately 2 and 6 km during KORUS-AQ [20,60]. Accordingly, the present results are consistent with a contribution from elevated or vertically decoupled coarse aerosol to large R. Nevertheless, because the POM-02 VSD is vertically integrated, this interpretation remains indirect and cannot by itself establish the altitude of the coarse-mode aerosol.

The spectral SSA provides an additional constraint on the optical properties of these aerosols (Figure 9). Median SSA generally increases with R across most wavelengths, with the largest differences observed at shorter wavelengths. At 400 nm, median SSA increases from 0.855 for R < 0.5 to 0.931 for R > 5.0, while at 500 nm it increases from 0.877 to 0.944. The corresponding differences become smaller at longer wavelengths toward the near-infrared. Although the substantial overlap in the interquartile ranges indicates that SSA alone does not distinctly separate the R regimes, the increase in regime medians suggests that the coarse-mode enhancement identified at high R is accompanied by a shift toward a more scattering-dominated column aerosol population. This behavior is consistent with previous observations of Asian dust over Korea. Measurements at Gosan during ACE-Asia showed higher SSA for a dust episode than for a regional pollution episode, and regional sun–sky radiometer analyses have also reported relatively high SSA for Asian dust transported to Korea and neighboring downwind regions [57,61].

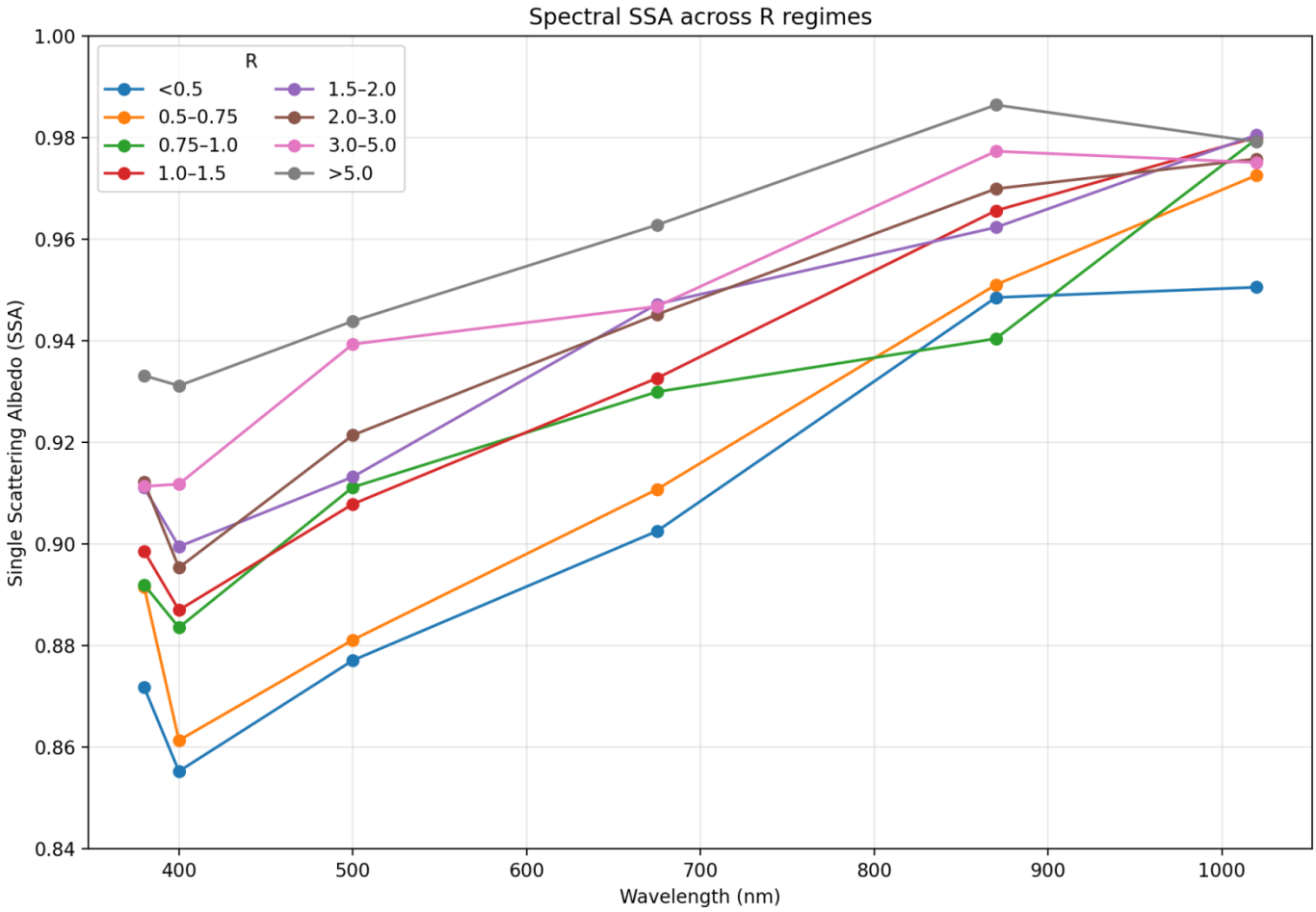


Figure 9. Spectral variation in SSA among the R bins during the investigation period.

Thus, the combined observations indicate that increasing R is accompanied by a systematic change in the column aerosol population, characterized by lower AE, enhanced coarse-mode volume, higher CMVF, and a more scattering-dominated optical character, while the corresponding response in surface PM_{10} remains weak. This combination suggests that the aerosol contributing to large ASH–PBLH discrepancies is increasingly dominated by coarse particles that are more strongly represented in the column than near the surface. Such optical and microphysical characteristics are compatible with the influence of mineral dust, particularly under springtime long-range transport conditions over East Asia. Previous observations over Korea have reported substantially lower AE and enhanced coarse-mode aerosol during Asian dust events [58], as well as vertically stratified aerosol structures associated with regional and transboundary transport [20,21]. However, because aerosol chemical composition and vertically resolved particle distributions are not directly measured in this study, mineral dust cannot be uniquely identified as the source of the observed high-R conditions. Rather, the present results indicate that R provides a useful measure of the degree to which column aerosol optical and microphysical properties differ from those represented by near-surface extinction.

4.2. Vertical Structure Classification Based on ASH-to-PBLH Ratio

Vertical structure is characterized using R defined in Equation (6), and three regimes are subsequently defined. Figure 10 shows the frequency distribution of R during the study period. The distribution is strongly right-skewed, with a median of 1.01 and first and third quartiles of 0.62 and 1.71, respectively. Although a substantial fraction of the observations is concentrated near R = 1, the pronounced upper tail shows that the relationship between ASH and PBLH varies considerably under different atmospheric conditions. Similar differences between column-integrated aerosol loading and boundary-layer structure have been reported over East Asia, where vertically heterogeneous and multilayer aerosol distributions are frequently observed [15,17]. Values of $R > 1$ indicate that the observed column aerosol loading is larger than the amount expected from the near-surface extinction uniformly distributed within the diagnosed PBL. These conditions therefore suggest additional aerosol loading above the near-surface layer or separation between the near-surface and upper aerosol layers. In contrast, $R < 1$ indicates that near-surface extinction is relatively large compared with the column-integrated aerosol loading, suggesting that aerosol extinction is concentrated in the lower portion of the boundary layer. These interpretations are consistent with previous vertically resolved observations that showed decreasing, well-mixed, and elevated or inverse profiles of aerosol extinction under different atmospheric conditions [14,15,17]. Based on this framework, three aerosol vertical-structure regimes are defined: a surface-dominated regime for $R < 0.75$, a well-coupled regime for $0.75 \leq R < 1.25$, and a column-enhanced/vertically decoupled regime for $R \geq 1.25$. These thresholds provide a symmetric range around R = 1 and are used as a practical classification rather than as a universal definition of aerosol vertical structure. The classification is then used to compare aerosol optical properties among the three regimes. To assess the robustness of the proposed classification, sensitivity analyses were conducted using alternative R thresholds and prescribed perturbations in ERA5 PBLH (Table S1). The results shows that the systematic increase in AOD and decrease in AE across the three regimes remained consistent under the tested conditions, while SSA exhibited a generally similar but less pronounced tendency. Although regime occurrence frequencies are sensitive to PBLH uncertainties, the overall relationships between R and aerosol optical properties are largely preserved.

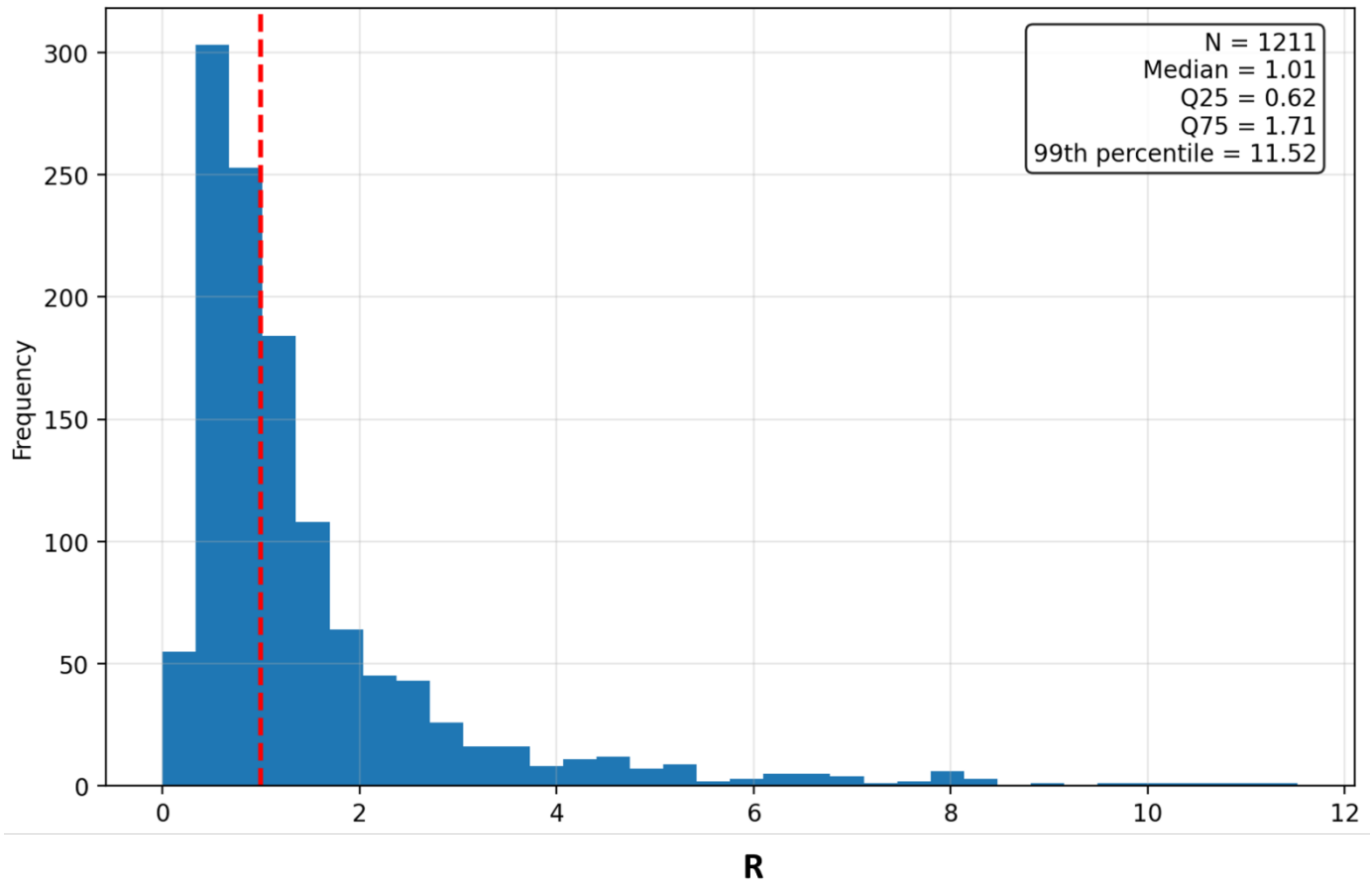


Figure 10. Frequency distribution of the ratio R during the investigation period with the median and quantiles. The red dashed line indicates R = 1.

Table 1 summarizes the aerosol optical and vertical-structure characteristics of the three regimes defined in Figure 10. The surface-concentrated regime (R < 0.75) has the lowest mean AOD_{500} (0.209 ± 0.092) and H_A (0.67 ± 0.29 km), while its mean PBLH is the highest among the three regimes (1.29 ± 0.46 km). In the well-coupled regime (0.75 ≤ R < 1.25), AOD_{500} rises to 0.312 ± 0.152 and H_A increases to 1.05 ± 0.40 km, while PBLH decreases to 1.08 ± 0.41 km. The nearly identical mean H_A and PBLH values in this regime indicate that the effective aerosol optical scale height is comparable to the diagnosed boundary-layer depth. In the column-enhanced/vertically decoupled regime (R ≥ 1.25), AOD_{500} further increases to 0.385 ± 0.199 and H_A increases to 1.47 ± 0.80 km, whereas PBLH decreases to 0.63 ± 0.38 km. This combination produces a clear separation between the aerosol optical scale height and the meteorological boundary-layer depth. The CS125 extinction coefficient varies only slightly among the three regimes. Its mean value decreases from 0.174 ± 0.145 km^{-1} in the surface-concentrated regime to 0.162 ± 0.107 km^{-1} in the well-coupled regime and 0.161 ± 0.071 km^{-1} in the column-enhanced/vertically decoupled regime. Thus, the increase in AOD_{500} from 0.209 to 0.385 is not accompanied by a corresponding increase in near-surface extinction. The rise in H_A therefore results primarily from greater column-integrated aerosol optical loading relative to the surface extinction coefficient, rather than from stronger aerosol extinction at the surface. $AE_{400–870}$ decreases systematically with increasing R, from 1.362 ± 0.255 in the surface-concentrated regime to 1.217 ± 0.285 in the well-coupled regime and 1.073 ± 0.333 in the column-enhanced/vertically decoupled regime. This decrease indicates a progressively weaker wavelength dependence of AOD and is consistent with an increasing relative contribution of coarse-mode particles to the atmospheric column. At the same time, SSA_{500} increases

progressively from 0.879 ± 0.070 to 0.899 ± 0.069 and 0.912 ± 0.065 across the three regimes. The combination of lower AE and higher SSA in the column-enhanced/vertically decoupled regime indicates that the enhanced column aerosol loading is associated with a coarser and less absorbing aerosol population than that in the surface-concentrated regime.

Table 1. Aerosol and vertical-structure characteristics for the three R regimes. N denotes the number of samples for each regime.

Regime	R	N	AOD_{500}	SSA_{500}	$AE_{400–870}$	$\beta_{ext,sfc}$ (km^{-1})	ASH_{870} (km)	PBLH (km)
Surface-concentrated	R < 0.75	427	0.209 ± 0.092	0.879 ± 0.070	1.362 ± 0.255	0.174 ± 0.145	0.665 ± 0.294	1.290 ± 0.463
Well-coupled	0.75 ≤ R < 1.25	326	0.312 ± 0.152	0.899 ± 0.069	1.217 ± 0.285	0.162 ± 0.107	1.051 ± 0.399	1.079 ± 0.405
Column-enhanced/vertically decoupled	R ≥ 1.25	458	0.385 ± 0.199	0.912 ± 0.065	1.073 ± 0.333	0.161 ± 0.071	1.467 ± 0.802	0.632 ± 0.375

To examine whether the aerosol vertical-structure classification derived from the ASH-to-PBLH ratio is consistent with independent vertical observations, CALIOP 532 nm and EarthCARE 355 nm aerosol extinction profiles are analyzed. The short overlap between the CALIOP record and the ground-based observation period limits the available comparisons. For the CALIOP case on 19 May 2023, 12 of the 20 examined profiles contain valid extinction retrievals. For EarthCARE, 255 files collected using a 50 km search radius around KIER represent 210 observations after duplicate processing versions are removed. Among the 107 daytime observations, 24 correspond temporally to available ground-based AOD measurements, and five contain valid lower-tropospheric extinction data. After cloud classification and missing vertical intervals are examined, two EarthCARE cases are selected for detailed comparison. The screening procedure is described in Supplementary Section S1.

On 19 May 2023, the ground-based ASH is 1.015 km and the ERA5 PBLH is 1.779 km, yielding R = 0.571, corresponding to the surface-concentrated regime. The CALIOP observations show aerosol extinction primarily between approximately 0.10 and 1.54 km altitude, within the planetary boundary layer (Figure S1). The maximum extinction coefficient is approximately 0.115 km^{-1} at an altitude of 1.24 km. The observed vertical distribution indicates that aerosols are primarily distributed within the planetary boundary layer rather than forming a distinct elevated aerosol layer above it. This result is consistent with the estimated ASH being smaller than the PBLH and supports the interpretation of the surface-concentrated regime based on the ASH-to-PBLH ratio. On 26 April 2025, the ground-based ASH values at 14:00 and 15:00 KST are 0.588 and 0.639 km, respectively, and the corresponding ERA5 PBLH values are 1.382 and 1.306 km, yielding R = 0.426–0.490. The EarthCARE profile shows its strongest aerosol extinction near the surface, with a maximum of approximately 0.372 km^{-1} at 0.23 km above ground (Figure S2a). Although additional extinction enhancements occur above the PBLH, they are weaker than the near-surface maximum. This distribution is qualitatively consistent with the surface-concentrated regime and illustrates that low R does not require the complete absence of aerosol above the PBLH. On 1 January 2026, the ground-based ASH is 3.153 km and the ERA5 PBLH is 1.175 km, yielding R = 2.683, corresponding to the column-enhanced regime. The EarthCARE profile shows lower-level aerosol signals together with an extinction enhancement at approximately 3.3–3.6 km above ground, well above the PBLH (Figure S2b). This upper-level enhancement is qualitatively consistent with the interpretation of an effective aerosol optical scale exceeding the boundary-layer depth.

Although only a small number of suitable cases remain after screening, these independent vertical observations show broad qualitative agreement with the R-based classification. The comparisons provide supporting case-study evidence rather than statistical validation, given the limited sample size, spatial separation, wavelength differences, and incomplete vertical retrieval coverage.

5. Conclusions

This study examines aerosol vertical structure over Daejeon, Korea, by combining near-surface extinction measurements with column-integrated aerosol optical properties and ERA5 PBLH. An effective ASH, H_A, is derived from AOD_{870} and the near-surface extinction coefficient, and its ratio to PBLH, R = H_A/PBLH, is used to quantify the relationship between the aerosol optical vertical extent and the meteorological boundary layer. The observed R distribution is strongly right-skewed, with a median of 1.01 and an interquartile range of 0.62–1.71, indicating that aerosol optical structure frequently departs from a simple condition in which column aerosol loading is vertically represented by the near-surface extinction distributed throughout the atmospheric boundary layer.

The relationship between H_A and PBLH exhibits pronounced seasonal variability. Spring shows the highest median R and the broadest upper range, indicating that conditions in which the effective aerosol optical extent exceeds the diagnosed PBLH occur frequently. Summer is characterized by a median R close to unity, whereas autumn shows the lowest median R, consistent with the preferential concentration of the aerosol extinction within the lower portion of the boundary layer. Winter exhibits intermediate R values with relatively large case-to-case variability. These results indicate that the meteorological mixing depth alone does not fully describe the vertical distribution of aerosol optical extinction.

A systematic relationship is also observed between R and column aerosol particle-size characteristics. $AE_{400–870}$ decreases with increasing R, while the VSD analysis independently shows a corresponding increase in the coarse-mode contribution. CMVF increases from approximately 0.50 at low R to nearly 0.68 at the highest R ranges, and this increase is driven primarily by an increase in V_c rather than by a reduction in V_f. In contrast, surface PM_{10} exhibits only a weak association with R. The different responses of columnar coarse-mode volume and surface PM_{10} indicate that increases in R are associated with progressively weaker coupling between surface aerosol conditions and the vertically integrated aerosol column. Spectral SSA simultaneously increases with R, particularly at shorter wavelengths, indicating that the coarse-mode enhancement at large R is accompanied by a shift toward a more scattering-dominated column aerosol population.

Based on R, the observations are classified into three regimes: surface-concentrated ($R < 0.75$), well-coupled ($0.75 \leq R < 1.25$), and column-enhanced/vertically decoupled ($R \geq 1.25$). Across these regimes, mean H_a increases from 0.67 to 1.47 km and AOD_{500} rises from 0.209 to 0.385, whereas mean PBLH decreases from 1.29 to 0.63 km. In contrast, the near-surface extinction coefficient remains nearly unchanged. The increase in H_A at large R therefore reflects enhanced column aerosol loading relative to near-surface extinction rather than stronger aerosol extinction at the ground. The simultaneous decrease in $AE_{400–870}$ and increase in SSA_{500} further indicate that the column-enhanced/vertically decoupled regime is characterized by a greater contribution from relatively coarse, more scattering aerosols.

These findings indicate that the ratio between ASH and PBLH provides a simple quantitative measure of surface–column aerosol coupling that cannot be obtained from AOD, surface extinction, or PBLH alone. In particular, large R values identify conditions where enhanced column aerosol loading and coarse-mode contributions are poorly represented by surface aerosol measurements. Although the column-integrated nature of the POM-02 retrieval does not directly determine the altitude of individual aerosol layers, the combined

behavior of H_A, PBLH, AE, VSD, SSA, and surface PM supports the use of R as an effective indicator of changes in aerosol vertical structure and surface–column decoupling.

Several limitations of this study should be acknowledged. The observation period spans approximately 33 months, and the availability of quality-controlled measurements varies considerably across months and seasons because sky-radiometer retrievals are restricted to cloud-free daytime conditions. Consequently, some seasonal statistics are based on relatively limited observations and may be influenced by individual years or specific atmospheric conditions. The reported seasonal differences should therefore be interpreted as characteristics of the present observational period rather than as established long-term climatological patterns. Longer-term observations with more uniform seasonal coverage would be beneficial for assessing the representativeness and robustness of these findings.

Supplementary Materials: The following supporting information can be downloaded at: https://www.mdpi.com/article/10.3390/rs18213640/s1, Figure S1: Comparison of CALIOP aerosol extinction observations with the ASH-based vertical-structure classification on 19 May 2023. (a) Along-track vertical distribution of the CALIOP 532 nm aerosol extinction coefficient, with latitude and longitude coordinates indicated along the horizontal axis. Colored markers represent valid extinction retrievals from 12 of the 20 profiles, while blank regions indicate unavailable retrievals. The red dashed vertical line indicates the nearest valid CALIOP profile to the KIER observation site. (b) Vertical profile of the 532 nm aerosol extinction coefficient at the nearest valid location (36.325° N, 126.112° E), approximately 112 km from KIER.; Figure S2. EarthCARE 355 nm aerosol extinction profiles for (a) 26 April 2025 (processing version vBa) and (b) 1 January 2026 (processing version vBc). Altitude is expressed above the local surface. Horizontal lines indicate the corresponding ERA5 PBLH values: 1.382 and 1.306 km for the 14:00 and 15:00 KST ground-based observations in panel (a), respectively, and 1.175 km for the 15:00 KST observation in panel (b). The corresponding ground-based R values are 0.426–0.490 and 2.683. Gray shading indicates cloud-classified bins. Cloud-classified and invalid retrievals are excluded from the extinction curves, and excluded intervals are not connected. Table S1: Sensitivity of aerosol vertical-structure classification and optical properties to alternative R thresholds and prescribed ERA5 PBLH perturbations; Table S2. Comparison of AOD, ASH, R, and regime sample sizes using measured AOD at 870 nm and interpolated AOD at 850 nm.; Table S3. Comparison of mean optical properties across the R regimes before and after wavelength interpolation [62].

Author Contributions: Conceptualization, C.K.K.; methodology, C.K.K.; software, C.K.K. and M.O.; validation, C.K.K. and M.O.; formal analysis, C.K.K.; investigation, C.K.K.; resources, C.K.K.; data curation, C.K.K., M.-G.K. and Y.B.; writing—original draft preparation, C.K.K.; writing—review and editing, C.K.K. and H.-G.K.; visualization, C.K.K. and M.O.; supervision, H.-G.K.; project administration, C.K.K. and H.-G.K.; funding acquisition, H.-G.K. All authors have read and agreed to the published version of the manuscript.

Funding: This study was conducted as part of the research and development program of the Korea Institute of Energy Research (C6-2403-15).

Data Availability Statement: The POM-02 sky radiometer data used in this study, including aerosol optical properties, are publicly available through the SKYNET International Data Center website https://www.skynet-isdc.org/ (accessed on 20 October 2026). Additional processed datasets and data supporting the findings of this study are available from the corresponding author upon reasonable request.

Acknowledgments: The authors gratefully acknowledge the support and cooperation of the SKYNET International Data Center (SKYNET ISDC) for providing access to the POM-02 sky radiometer data used in this study. During the preparation of this manuscript, the authors used OpenAI's ChatGPT (GPT-5) to generate the graphical abstract. The authors reviewed and edited the output and assume full responsibility for the content of this publication.

Conflicts of Interest: The authors declare no conflicts of interest.

Abbreviations

The following abbreviations are used in this manuscript:

AE	Ångström Exponent
AERONET	Aerosol Robotic Network
AOD	Aerosol Optical Depth
ASH	Aerosol Scale Height
CALIPSO	Cloud-Aerosol Lidar and Infrared Pathfinder Satellite Observations
CATS	Cloud-Aerosol Transport System
CMVF	Coarse-mode Volume Fraction
ECMWF	European Centre for Medium-Range Weather Forecasts
ERA5	Fifth-generation ECMWF Atmospheric Reanalysis
IFS	Integrated Forecasting System
IQR	Interquartile Range
KIER	Korea Institute of Energy Research
KORUS-AQ	Korea–United States Air Quality Study
LST	Local Standard Time
MOR	Meteorological Optical Range
NAMIS	National Ambient Air Quality Information Management System
NIER	National Institute of Environmental Research
PBL	Planetary Boundary Layer
PBLH	Planetary Boundary Layer Height
RH	Relative Humidity
SSA	Single Scattering Albedo
UTC	Coordinated Universal Time
V_c	Coarse-mode Aerosol Volume
V_f	Fine-mode Aerosol Volume
VSD	Volume Size Distribution

Appendix A

Appendix A.1. Figure A1

The fine–coarse separation radius is determined from the overall median volume size distribution derived from all valid observations. The local minimum between the fine- and coarse-mode peaks occurs at a particle radius of 0.595 µm, which is used as the cutoff for calculating fine- and coarse-mode aerosol volumes.

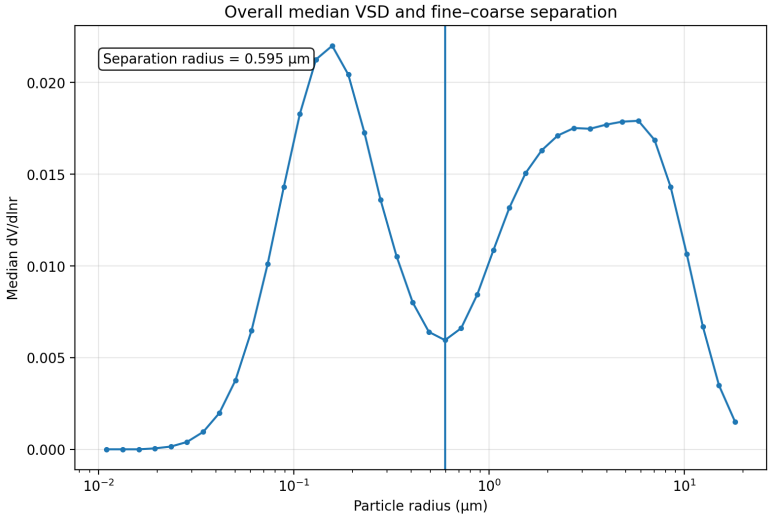


Figure A1. Overall median aerosol volume size distribution and fine–coarse-mode separation defined by a particle radius of 0.595 µm. Vertical bar indicates the threshold radius to divide two regimes.

Appendix A.2. Figure A2

The relationship between the median R and median surface PM_{10} concentration across the R interval shows only a weak association. The regression based on the binned median values yields $\gamma^2 = 0.166$, indicating that changes in R are only weakly reflected by surface PM_{10} concentrations.

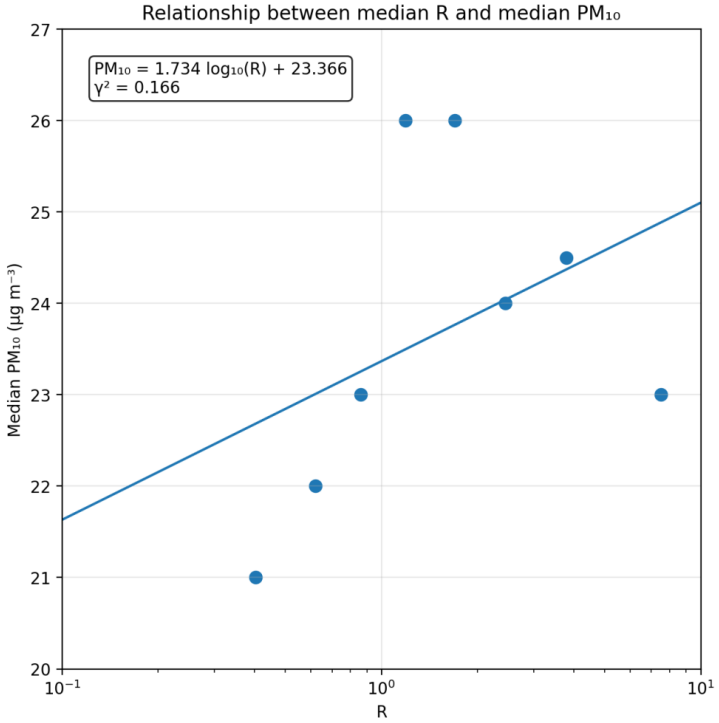


Figure A2. Scatter plot of the median R against the median surface PM_{10} concentration for each R interval.

References

1. Forster, P.; Storelvmo, T.; Armour, K.; Collins, W.; Dufresne, J.L.; Frame, D.; Lunt, D.J.; Mauritsen, T.; Palmer, M.D.; Watanabe, M.; et al. The Earth's energy budget, climate feedbacks and climate sensitivity. In *Climate Change—The Physical Science Basis: Working Group I Contribution to the Sixth Assessment Report of the Intergovernmental Panel on Climate Change*; Intergovernmental Panel on Climate Change, Ed.; Cambridge University Press: Cambridge, UK, 2021; pp. 923–1054.
2. Li, Z.; Guo, J.; Ding, A.; Liao, H.; Liu, J.; Sun, Y.; Wang, T.; Xue, H.; Zhang, H.; Zhu, B. Aerosol and boundary-layer interactions and impact on air quality. *Natl. Sci. Rev.* **2017**, *4*, 810–833. [CrossRef]
3. Bellouin, N.; Quaas, J.; Gryspeerdt, E.; Kinne, S.; Stier, P.; Watson-Parris, D.; Boucher, O.; Carslaw, K.S.; Christensen, M.; Daniau, A.L.; et al. Bounding global aerosol radiative forcing of climate change. *Rev. Geophys.* **2020**, *58*, e2019RG000660. [CrossRef] [PubMed]
4. Kim, D.-H.; Sohn, B.-J.; Nakajima, T.; Takamura, T.; Takemura, T.; Choi, B.-C.; Yoon, S.-C. Aerosol optical properties over east Asia determined from ground-based sky radiation measurements. *J. Geophys. Res.* **2004**, *109*, D02209. [CrossRef]
5. Koo, J.-H.; Kim, J.; Kim, M.-J.; Cho, H.K.; Aoki, K.; Yamano, M. Analysis of aerosol optical properties in Seoul using skyradiometer observation. *Atmos. Korea* **2007**, *17*, 407–420. (In Korean with English Abstract)
6. Kim, S.-W.; Yoon, S.-C.; Kim, J.; Kim, S.-Y. Seasonal and monthly variations of columnar aerosol optical properties over east Asia determined from multi-year MODIS, LIDAR, and AERONET Sun/sky radiometer measurements. *Atmos. Environ.* **2007**, *41*, 1634–1651. [CrossRef]
7. Chun, Y.; Cho, H.-K.; Chung, H.-S.; Lee, M. Historical records of Asian Dust events (Hwangsa) in Korea. *Bull. Am. Meteorol. Soc.* **2008**, *89*, 823–828. [CrossRef]
8. Lee, J.; Kim, J.; Song, C.H.; Kim, S.B.; Chun, Y.; Sohn, B.J.; Holben, B.N. Characteristics of aerosol types from AERONET sunphotometer measurements. *Atmos. Environ.* **2010**, *44*, 3110–3117. [CrossRef]

9. Koo, J.-H.; Kim, J.; Lee, J.; Eck, T.F.; Lee, Y.G.; Park, S.S.; Kim, M.; Jung, U.; Yoon, J.; Mok, J.; et al. Wavelength dependence of Ångström exponent and single scattering albedo observed by skyradiometer in Seoul, Korea. *Atmos. Res.* **2016**, *181*, 12–19. [CrossRef]
10. Zhai, S.; Jacob, D.J.; Brewer, J.F.; Li, K.; Moch, J.M.; Kim, J.; Lee, S.; Lim, H.; Lee, H.C.; Kuk, S.K.; et al. Relating geostationary satellite measurements of aerosol optical depth (AOD) over East Asia to fine particulate matter ($PM_{2.5}$): Insights from the KORUS-AQ aircraft campaign and GEOS-Chem model simulations. *Atmos. Chem. Phys.* **2021**, *21*, 16775–16791. [CrossRef]
11. Gui, L.; Tao, M.; Wang, Y.; Wang, L.; Chen, L.; Lin, C.; Tao, J.; Wang, J.; Yu, C. Climatology of aerosol types and their vertical distribution over East Asia based on CALIPSO lidar measurements. *Int. J. Climatol.* **2022**, *42*, 6042–6054. [CrossRef]
12. Kang, S.; An, C.; Lee, D.; Jung, D.-H.; Jeong, E.; Jeong, J.; Song, I.-H.; Shin, H.J.; Lee, S.-H.; Jung, H.-J.; et al. Analysis of air quality based on national monitoring networks in the Republic of Korea, 2023—Annual trends in air quality over two decades in South Korea. *Asian J. Atmos. Environ.* **2025**, *19*, 28. [CrossRef]
13. Lin, J.; van Donkelaar, A.; Xin, J.; Che, H.; Wang, Y. Clear-sky aerosol optical depth over East China estimated from visibility measurements and chemical transport modeling. *Atmos. Environ.* **2014**, *95*, 258–267. [CrossRef]
14. Chew, B.N.; Campbell, J.R.; Hyer, E.J.; Salinas, S.V.; Reid, J.S.; Welton, E.J.; Holben, B.N.; Liew, S.C. Relationship between aerosol optical depth and particulate matter over Singapore: Effects of aerosol vertical distributions. *Aerosol Air Qual. Res.* **2016**, *16*, 2818–2830. [CrossRef] [PubMed]
15. Zhang, J.; Wang, S.; Guo, Y.; Zhang, R.; Qin, X.; Huang, K.; Wang, D.; Fu, Q.; Wang, J.; Zhou, B. Aerosol vertical profile retrieved from ground-based MAX-DOAS observation and characteristic distribution during wintertime in Shanghai, China. *Atmos. Environ.* **2018**, *192*, 193–205. [CrossRef]
16. Cheng, Y.; Dai, T.; Li, J.; Shi, G. Measurement Report: Determination of aerosol vertical features on different timescales over East Asia based on CATS aerosol products. *Atmos. Chem. Phys.* **2020**, *20*, 15307–15322. [CrossRef]
17. Su, T.; Li, Z.; Li, C.; Li, J.; Han, W.; Shen, C.; Tan, W.; Wei, J.; Guo, J. The significant impact of aerosol vertical structure on lower atmosphere stability and its critical role in aerosol–planetary boundary layer (PBL) interactions. *Atmos. Chem. Phys.* **2020**, *20*, 3713–3724. [CrossRef]
18. Qiu, J.; Zong, X.; Zhang, X. A study of the scaling height of the tropospheric aerosol and its extinction coefficient profile. *J. Aerosol Sci.* **2005**, *36*, 361–371. [CrossRef]
19. Shin, S.-K.; Lee, K.-H. Modelling of aerosol vertical distribution during a spring season at Gwangju, Korea. *Asian J. Atmos. Environ.* **2016**, *10*, 13–21. [CrossRef]
20. Peterson, D.A.; Hyer, E.J.; Han, S.-O.; Crawford, J.H.; Park, R.J.; Holz, R.; Kuehn, R.E.; Eloranta, E.; Knote, C.; Jordan, C.E.; et al. Meteorology influencing springtime air quality, pollution transport, and visibility in Korea. *Elem. Sci. Anthr.* **2019**, *7*, 57. [CrossRef]
21. LeBlanc, S.E.; Segal-Rozenhaimer, M.; Redemann, J.; Flynn, C.; Johnson, R.R.; Dunagan, S.E.; Dahlgren, R.; Kim, J.; Choi, M.; da Silva, A.; et al. Airborne observations during KORUS-AQ show that aerosol optical depths are more spatially self-consistent than aerosol intensive properties. *Atmos. Chem. Phys.* **2022**, *22*, 11275–11304. [CrossRef]
22. Zhang, Z.; Mu, L.; Li, C. Comparison of planetary boundary layer height derived from lidar in AD-Net and ECMWFs reanalysis data over East Asia. *Atmosphere* **2022**, *13*, 1976. [CrossRef]
23. Lee, S.; Lee, S.-J.; Kang, J.-H.; Jang, E.-S. Spatial and temporal variations in atmospheric ventilation index coupled with particulate matter concentration in South Korea. *Sustainability* **2021**, *13*, 8954. [CrossRef]
24. Brock, C.A.; Wagner, N.L.; Anderson, B.E.; Beyersdorf, A.; Campuzano-Jost, P.; Day, D.A.; Diskin, G.S.; Gordon, T.D.; Jimenez, J.L.; Lack, D.A.; et al. Aerosol optical properties in the southeastern United States in summer—Part 2: Sensitivity of aerosol optical depth to relative humidity and aerosol parameters. *Atmos. Chem. Phys.* **2016**, *16*, 5009–5019. [CrossRef]
25. Liu, Q.; Liu, D.; Gao, Q.; Tian, P.; Wang, F.; Zhao, D.; Bi, K.; Wu, Y.; Ding, S.; Hu, K.; et al. Vertical characteristics of aerosol hygroscopicity and impacts on optical properties over the North China Plain during winter. *Atmos. Chem. Phys.* **2020**, *20*, 3931–3944. [CrossRef]
26. Nakajima, T.; Campanelli, M.; Che, H.; Estellés, V.; Irie, H.; Kim, S.-W.; Kim, J.; Liu, D.; Nishizawa, T.; Pandithurai, G.; et al. An overview of and issues with sky radiometer technology and Skynet. *Atmos. Meas. Tech.* **2020**, *13*, 4195–4218. [CrossRef]
27. Nakajima, T.; Tonna, G.; Rao, R.; Boi, P.; Kaufman, Y.; Holben, B. Use of sky brightness measurements from ground for remote sensing of particulate polydispersions. *Appl. Opt.* **1996**, *35*, 2672–2686. [CrossRef] [PubMed]
28. Khatri, P.; Takamura, T. An algorithm to screen cloud-A?ected data for sky radiometer data analysis. *J. Meteorol. Soc. Jpn.* **2009**, *87*, 189–204. [CrossRef]
29. Kaufman, Y.J.; Gobbi, G.P.; Koren, I. Aerosol climatology using a tunable spectral variability cloud screening of AERONET data. *Geophys. Res. Lett.* **2006**, *33*, L07817. [CrossRef]
30. Smirnov, A.; Holben, B.N.; Eck, T.F.; Dubovik, O.; Slutsker, I. Cloud-screening and quality control algorithms for the AERONET database. *Remote Sens. Environ.* **2000**, *73*, 337–349. [CrossRef]

31. Jiang, Z.; Duan, M.; Che, H.; Zhang, W.; Nakajima, T.; Hashimoto, M.; Chen, B.; Yamazaki, A. Intercomparison between the aerosol optical properties retrieved by different inversion methods from Skynet sky radiometer observations over Qionghai and Yucheng in China. *Atmos. Meas. Tech.* **2020**, *13*, 1195–1212. [CrossRef]
32. Hashimoto, M.; Nakajima, T.; Dubovik, O.; Campanelli, M.; Che, H.; Khatri, P.; Takamura, T.; Pandithurai, G. Development of a new data-processing method for Skynet sky radiometer observations. *Atmos. Meas. Tech.* **2012**, *5*, 2723–2737. [CrossRef]
33. Hersbach, H.; Bell, B.; Berrisford, P.; Hirahara, S.; Horányi, A.; Muñoz-Sabater, J.; Nicolas, J.; Peubey, C.; Radu, R.; Schepers, D.; et al. The ERA5 global reanalysis. *Q. J. R. Meteorol. Soc.* **2020**, *146*, 1999–2049. [CrossRef]
34. Vogelezang, D.H.P.; Holtslag, A.A.M. Evaluation and model impacts of alternative boundary-layer height formulations. *Bound.-Layer Meteorol.* **1996**, *81*, 245–269. [CrossRef]
35. Eck, T.F.; Holben, B.N.; Dubovik, O.; Smirnov, A.; Goloub, P.; Chen, H.B.; Chatenet, B.; Gomes, L.; Zhang, X.Y.; Tsay, S.C.; et al. Columnar aerosol optical properties at AERONET sites in central eastern Asia and aerosol transport to the tropical mid-Pacific. *J. Geophys. Res.* **2005**, *110*, D06202. [CrossRef]
36. Eck, T.F.; Holben, B.N.; Reid, J.S.; Xian, P.; Giles, D.M.; Sinyuk, A.; Smirnov, A.; Schafer, J.S.; Slutsker, I.; Kim, J.; et al. Observations of the interaction and transport of fine mode aerosols with cloud and/or fog in NorthEast Asia from aerosol robotic network and satellite remote sensing. *J. Geophys. Res. Atmos.* **2018**, *123*, 5560–5587. [CrossRef] [PubMed]
37. Shin, S.K.; Tesche, M.; Noh, Y.; Müller, D. Aerosol-type classification based on AERONET version 3 inversion products. *Atmos. Meas. Tech.* **2019**, *12*, 3789–3803. [CrossRef]
38. Jung, J.; Kim, Y.J.; Lee, K.Y.; -Cayetano, M.G.; Batmunkh, T.; Koo, J.H.; Kim, J. Spectral optical properties of long-range transport Asian dust and pollution aerosols over NorthEast Asia in 2007 and 2008. *Atmos. Chem. Phys.* **2010**, *10*, 5391–5408. [CrossRef]
39. Noh, Y.M.; Müller, D.; Lee, H.; Lee, K.; Kim, Y.J. Columnar aerosol optical and radiative properties according to season and air mass transport pattern over East Asia. *Environ. Monit. Assess.* **2012**, *184*, 4763–4775. [CrossRef] [PubMed]
40. Schuster, G.L.; Dubovik, O.; Holben, B.N. Angstrom exponent and bimodal aerosol size distributions. *J. Geophys. Res.* **2006**, *111*, D07207. [CrossRef]
41. Koo, J.-H.; Lee, J.; Kim, J.; Eck, T.F.; Giles, D.M.; Holben, B.N.; Park, S.S.; Choi, M.; Kim, N.; Yoon, J.; et al. Investigation of the relationship between the fine mode fraction and Ångström exponent: Cases in Korea. *Atmos. Res.* **2021**, *248*, 105217. [CrossRef]
42. Hamill, P.; Giordano, M.; Ward, C.; Giles, D.; Holben, B. An AERONET-based aerosol classification using the Mahalanobis distance. *Atmos. Environ.* **2016**, *140*, 213–233. [CrossRef]
43. Sinyuk, A.; Holben, B.N.; Eck, T.F.; Giles, D.M.; Slutsker, I.; Korkin, S.; Schafer, J.S.; Smirnov, A.; Sorokin, M.; Lyapustin, A. The AERONET Version 3 aerosol retrieval algorithm, associated uncertainties and comparisons to Version 2. *Atmos. Meas. Tech.* **2020**, *13*, 3375–3411. [CrossRef]
44. Dubovik, O.; Smirnov, A.; Holben, B.N.; King, M.D.; Kaufman, Y.J.; Eck, T.F.; Slutsker, I. Accuracy assessments of aerosol optical properties retrieved from Aerosol Robotic Network (AERONET) Sun and sky radiance measurements. *J. Geophys. Res.* **2000**, *105*, 9791–9806. [CrossRef]
45. Mok, J.; Krotkov, N.A.; Torres, O.; Jethva, H.; Li, Z.; Kim, J.; Koo, J.H.; Go, S.; Irie, H.; Labow, G.; et al. Comparisons of spectral aerosol single scattering albedo in Seoul, South Korea. *Atmos. Meas. Tech.* **2018**, *11*, 2295–2311. [CrossRef]
46. Han, H.; Kim, G.; Seo, H.; Shin, K.H.; Lee, D.H. Significant seasonal changes in optical properties of brown carbon in the midlatitude atmosphere. *Atmos. Chem. Phys.* **2020**, *20*, 2709–2718. [CrossRef]
47. Choi, Y.; Ghim, Y.S.; Zhang, Y.; Park, S.-M.; Song, I.-H. Estimation of surface concentrations of black carbon from long-term measurements at Aeronet sites over Korea. *Remote Sens.* **2020**, *12*, 3904. [CrossRef]
48. Eom, S.; Kim, J.; Lee, S.; Holben, B.N.; Eck, T.F.; Park, S.-B.; Park, S.S. Long-term variation of aerosol optical properties associated with aerosol types over East Asia using AERONET and satellite (VIIRS, OMI) data (2012–2019). *Atmos. Res.* **2022**, *280*, 106457. [CrossRef]
49. Eck, T.F.; Holben, B.N.; Kim, J.; Beyersdorf, A.J.; Choi, M.; Lee, S.; Koo, J.-H.; Giles, D.M.; Schafer, J.S.; Sinyuk, A.; et al. Influence of cloud, fog, and high relative humidity during pollution transport events in South Korea: Aerosol properties and PM2.5 variability. *Atmos. Environ.* **2020**, *232*, 117530. [CrossRef]
50. Giles, D.M.; Holben, B.N.; Eck, T.F.; Sinyuk, A.; Smirnov, A.; Slutsker, I.; Dickerson, R.R.; Thompson, A.M.; Schafer, J.S. An analysis of AERONET aerosol absorption properties and classifications representative of aerosol source regions. *J. Geophys. Res.* **2012**, *117*, D17203. [CrossRef]
51. Lee, S.; Hong, J.; Cho, Y.; Choi, M.; Kim, J.; Park, S.S.; Ahn, J.-Y.; Kim, S.-K.; Moon, K.-J.; Eck, T.F.; et al. Characteristics of classified aerosol types in South Korea during the MAPS-Seoul campaign. *Aerosol Air Qual. Res.* **2018**, *18*, 2195–2206. [CrossRef]
52. Lee, H.-J.; Jo, H.-Y.; Kim, S.-W.; Park, M.-S.; Kim, C.-H. Impacts of atmospheric vertical structures on transboundary aerosol transport from China to South Korea. *Sci. Rep.* **2019**, *9*, 13040. [CrossRef] [PubMed]
53. Oak, Y.J.; Jacob, D.J.; Pendergrass, D.C.; Dang, R.; Colombi, N.K.; Chong, H.; Lee, S.; Kuk, S.K.; Kim, J. Air quality trends and regimes in South Korea inferred from 2015–2023 surface and satellite observations. *Atmos. Chem. Phys.* **2025**, *25*, 3233–3252. [CrossRef]

54. Kim, S.-W.; Yoon, S.-C.; Kim, J.; Kang, J.-Y.; Sugimoto, N. Asian dust event observed in Seoul, Korea, during 29–31 May 2008: Analysis of transport and vertical distribution of dust particles from lidar and surface measurements. *Sci. Total Environ.* **2010**, *408*, 1707–1718. [CrossRef] [PubMed]
55. Liu, D.; Zhao, T.; Boiyo, R.; Chen, S.; Lu, Z.; Wu, Y.; Zhao, Y. Vertical structures of dust aerosols over East Asia based on CALIPSO retrievals. *Remote Sens.* **2019**, *11*, 701. [CrossRef]
56. Matsuki, A.; Iwasaka, Y.; Osada, K.; Matsunaga, K.; Kido, M.; Inomata, Y.; Trochkine, D.; Nishita, C.; Nezuka, T.; Sakai, T.; et al. Seasonal dependence of the long-range transport and vertical distribution of free tropospheric aerosols over east Asia: On the basis of aircraft and lidar measurements and isentropic trajectory analysis. *J. Geophys. Res.* **2003**, *108*, 8663. [CrossRef]
57. Yu, X.; Cheng, T.; Chen, J.; Liu, Y. A comparison of dust properties between China continent and Korea, Japan in East Asia. *Atmos. Environ.* **2006**, *40*, 5787–5797. [CrossRef]
58. Kim, S.-W.; Yoon, S.-C.; Kim, J. Columnar Asian dust particle properties observed by sun/sky radiometers from 2000 to 2006 in Korea. *Atmos. Environ.* **2008**, *42*, 492–504. [CrossRef]
59. Kim, J.-M.; Lee, H.-J.; Jo, H.-Y.; Jo, Y.-J.; Kim, C.-H. Vertical characteristics of secondary aerosols observed in the Seoul and Busan metropolitan areas of Korea during KORUS-AQ and associations with meteorological conditions. *Atmosphere* **2021**, *12*, 1451. [CrossRef]
60. Saide, P.E.; Gao, M.; Lu, Z.; Goldberg, D.L.; Streets, D.G.; Woo, J.H.; Beyersdorf, A.; Corr, C.A.; Thornhill, K.L.; Anderson, B.; et al. Understanding and improving model representation of aerosol optical properties for a Chinese haze event measured during KORUS-AQ. *Atmos. Chem. Phys.* **2020**, *20*, 6455–6478. [CrossRef]
61. Kim, S.-W.; Yoon, S.-C.; Jefferson, A.; Ogren, J.A.; Dutton, E.G.; Won, J.-G.; Ghim, Y.S.; Lee, B.-I.; Han, J.-S. Aerosol optical, chemical and physical properties at Gosan, Korea during Asian dust and pollution episodes in 2001. *Atmos. Environ.* **2005**, *39*, 39–50. [CrossRef]
62. Kim, M.-H.; Kim, S.-W.; Yoon, S.-C.; Omar, A.H. Comparison of aerosol optical depth between CALIOP and MODIS-Aqua for CALIOP aerosol subtypes over the ocean. *J. Geophys. Res.* **2013**, *118*, 13241–13252. [CrossRef]

Disclaimer/Publisher's Note: The statements, opinions and data contained in all publications are solely those of the individual author(s) and contributor(s) and not of MDPI and/or the editor(s). MDPI and/or the editor(s) disclaim responsibility for any injury to people or property resulting from any ideas, methods, instructions or products referred to in the content.